Universal Critical Density: Cross-Scale Consistency of ρ_T

Matthew Lukin Smawfield

Version: v0.5 (New Delhi)

First published: 28 December 2025 · Last updated: 7 June 2026

DOI: 10.5281/zenodo.18064365

Abstract

Dark matter observations across cosmological scales exhibit a regularity: the characteristic radius at which Newtonian dynamics fails scales as $R \propto M^{1/3}$, implying a universal critical proximity scale, observationally proxied by ρ_T. This scaling appears in galaxy rotation curves (SPARC database), ultra-diffuse galaxies (DF2/DF4), and the Milky Way's dark-matter onset. This pattern is interpreted within TEP as a candidate saturation scale in the conformal time-field sector of the Temporal Equivalence Principle (TEP), where field saturation occurs at a characteristic proximity scale, observationally proxied by the density ρ_T; a soliton interpretation is one candidate microscopic realization.

Terrestrial calibration—derived from a newly identified distance-structured correlation in GNSS atomic clocks—provides an empirical anchor. Multi-center analysis (CODE, IGS, ESA) reveals correlations with characteristic length $L_c \approx 4200$ km for Earth's mass ($M_\oplus \approx 6 \times 10^{27}$ g). The characteristic length L_c is interpreted as the Temporal Topology saturation radius for Earth's mass; a soliton interpretation is one candidate microscopic realization, not assumed in the calibration. This implies $\rho_T \approx 20$ g/cm³. This calibration exhibits 25-year temporal stability and survives raw RINEX validation, constraining processing-artifact explanations.

Galactic-scale validation comes from the SPARC rotation curve database (167 galaxies). The empirical dark matter onset scaling is $\alpha_{\mathrm{SPARC}} = 0.355 \pm 0.043$ (bootstrap, 1000 resamples), consistent with the $M^{1/3}$ expectation within $\sim$0.5σ. For the Milky Way, the SPARC-calibrated $M^{1/3}$ relation predicts a dark-matter onset radius $R_{\mathrm{DM}} \approx 3$ kpc, consistent with the observed transition from baryonic to dark-matter-dominated rotation at $R \sim 3$–5 kpc. For ultra-diffuse galaxies DF2 and DF4, the model predicts Temporal Topology saturation radii exceeding tidal radii, consistent with observed dark matter deficiency via tidal stripping of the scalar field envelope.

Temporal Topology screening resolves the apparent conflict with precision GR tests. Analysis of 26 astrophysical objects spanning 15 orders of magnitude in density reveals a consistency relation $S \propto \rho^{1/3}$, algebraically expected from the $R_T(M)$ construction; it explains why GR tests pass (binary pulsars: $S \sim 29{,}000$) while galactic dynamics ($\rho \sim 10^{-24}$ g/cm³, $S \sim 0.01$) exhibit strong scalar effects.

The saturation density $\rho_T \approx 20$ g/cm³ emerges as a candidate universal saturation scale of the temporal-field topology — not an ambient-density switch — supported by cross-scale consistency across 18 orders of magnitude in mass (Earth to galaxy), within stated uncertainties. This externally calibrated value enables tightly constrained astrophysical applications, including the RBH-1 runaway black hole candidate (Smawfield 2025h, Paper 7).

The $\rho^{1/3}$ hierarchy is a consistency relation induced by the $R_T(M)$ construction; it is not, by itself, an independent discriminator of microscopic screening mechanism.

Keywords: dark matter – gravitation – scalar fields – galaxies: kinematics and dynamics – temporal equivalence principle

1. Introduction: The Dark Matter Problem as a Temporal Structure Problem

The Universal Scaling Anomaly

Dark matter observations across cosmological scales reveal an empirical regularity. From dwarf galaxies ($M \sim 10^9 M_\odot$) to galaxy clusters ($M \sim 10^{15} M_\odot$), the characteristic radius at which Newtonian dynamics fails—the "dark matter onset"—scales approximately as $R \propto M^{1/3}$. This implies a universal critical proximity scale, observationally proxied by $\rho_T \sim M/R^3 \sim \text{constant}$, at which gravitational phenomenology changes.

This scaling appears in multiple independent contexts:

- **Galaxy rotation curves:** SPARC database analysis yields $R_{\rm DM} \propto M^{\alpha_{\rm SPARC}}$ with $\alpha_{\rm SPARC} = 0.355 \pm 0.043$ (bootstrap, 1000 resamples; Lelli et al. 2016; this work).
- **Ultra-diffuse galaxies:** DF2 and DF4 exhibit dark matter deficiency consistent with saturation radii exceeding tidal radii (van Dokkum et al. 2018, 2019).
- **Milky Way:** The SPARC-calibrated $M^{1/3}$ relation predicts a dark-matter onset at $R_{\rm DM} \approx 3$ kpc for the Milky Way, consistent with the observed transition from baryonic to dark-matter-dominated rotation at $R \sim 3$–5 kpc (Gaia Collaboration 2023; Sofue 2020).

The persistence of this $M^{1/3}$ scaling across 6 orders of magnitude in mass and 15 orders of magnitude in density suggests a fundamental physical scale, not a coincidence of baryonic feedback or halo assembly.

Reframing Dark Matter: Phantom Mass from Temporal Shear

The Temporal Equivalence Principle (TEP) proposes that gravitational phenomena arise from a conformal time field $\phi(x^\mu)$ that modulates proper time rates. This phenomenology arises from the TEP action (Smawfield 2025a, Paper 0):

$$S = \int d^4x \sqrt{-g} \left[\frac{M_{\rm Pl}^2}{2} R - \frac{1}{2}(\partial\phi)^2 - V(\phi) \right] + S_m[\tilde{g}_{\mu\nu}] \tag{1}$$

where matter couples to the Jordan frame metric $\tilde{g}_{\mu\nu} = A^2(\phi) g_{\mu\nu} + B(\phi) \nabla_\mu \phi \nabla_\nu \phi$. At late times, $B(\phi)$ is strongly constrained by multi-messenger observations and can be neglected, yielding $\tilde{g}_{\mu\nu} \approx A^2(\phi) g_{\mu\nu}$ with $A(\phi) = \exp(\beta_A \phi / M_{\rm Pl})$. The scalar saturation potential $V(\phi)$ prevents the gradient from diverging, leading to field saturation at characteristic density ρ_T. In this framework, the "dark matter" problem is reinterpreted as a violation of the *isochrony axiom*—the assumption that clocks at the same gravitational potential tick at the same rate regardless of their spatial separation or the mass distribution's history.

When this axiom is relaxed, gravitational lensing and dynamical mass estimates diverge. Light propagation depends on the *integrated* time dilation along the null geodesic, while orbital dynamics depend on the *local* time gradient. This creates "phantom mass"—an apparent excess in lensing mass relative to dynamical mass—without invoking non-baryonic particles.[†]

[†]*Note: This geometric "phantom mass" from temporal shear differs from cosmological "phantom energy" (dark energy with $w < -1$). The former arises from spatial gradients in proper time; the latter from exotic equation-of-state matter.*

The characteristic scale at which this temporal structure becomes significant is set by the saturation scale ρ_T, where the scalar field ϕ reaches its self-interaction threshold and saturates—forming a stable, localized configuration (a soliton under that interpretation) with radius:

$$R_T = \left(\frac{3M}{4\pi\rho_T} \right)^{1/3}. \tag{2}$$

This $M^{1/3}$ scaling is a direct consequence of the saturation condition; under a soliton interpretation, this corresponds to soliton formation.

The Multi-Scale Validation Strategy

This paper establishes ρ_T through a convergent multi-scale approach:

Table 1: Cross-Scale Validation of ρ_T

Scale	System	Mass Range	Density Range	Key Observable	Result
Terrestrial	GNSS Clocks	$M_\oplus \sim 6 \times 10^{27}$ g	$\rho_\oplus \sim 5.5$ g/cm³	$L_c \approx 4200$ km	$\rho_T \approx 20$ g/cm³
Galactic	SPARC Galaxies	10^9–$10^{12} M_\odot$	$\rho \sim 10^{-24}$ g/cm³	$R_{\rm DM} \propto M^{\alpha_{\rm SPARC}}$	$\alpha_{\rm SPARC} = 0.355 \pm 0.043$
Local	Milky Way	$M_{\rm bar} \sim 6 \times 10^{10} M_\odot$	$\rho \sim 10^{-24}$ g/cm³	Inner mass-discrepancy onset	$R_{\rm DM} \approx 3$ kpc (observed ∼3–5 kpc)
Screening	26 Objects	10^{-24}–10^{33} g	10^{-24}–10^{14} g/cm³	$S \propto \rho^{\beta_{\rm scr}}$	$\beta_{\rm scr} = 0.334$ ($R^2 = 0.99995$)

Note: The convergence of constraints across 18 orders of magnitude in mass (Earth to galaxy) motivates ρ_T as a candidate saturation scale.

Paper Structure

The remainder of this paper is organized as follows:

- **Section 2:** Terrestrial calibration via GNSS atomic clock correlations, establishing $L_c \approx 4200$ km → $\rho_T \approx 20$ g/cm³.
- **Section 3:** Galactic validation via SPARC rotation curves, confirming $M^{1/3}$ scaling.
- **Section 4:** Screening hierarchy analysis, explaining why GR tests pass despite scalar field presence.
- **Section 5:** Physical constraints on ρ_T, including electron degeneracy, the Thomas–Fermi bridge, and dimensional analysis.
- **Section 6:** The Universal Scaling Law, synthesizing constraints across all regimes.
- **Section 7:** Milky Way dark-matter onset at $R_{\rm DM} \approx 3$ kpc.
- **Section 8:** Discussion of dark matter as phantom mass and cosmological implications.
- **Section 9:** Conclusion and astrophysical applications (including RBH-1, companion paper).

This multi-scale convergence establishes $\rho_T \approx 20$ g/cm³ as an externally calibrated parameter (with explicit systematic uncertainty), enabling sharply constrained astrophysical applications such as the RBH-1 runaway black hole candidate (Smawfield 2025h, Paper 7).

2. Terrestrial Calibration: GNSS Atomic Clock Correlations

Distance-Structured Correlations in Atomic Clocks

The first empirical constraint on ρ_T comes from terrestrial atomic clock networks. Multi-center analysis of GNSS (Global Navigation Satellite System) clock products reveals distance-structured correlations with a characteristic length scale $L_c \approx 4200$ km for Earth's mass. Operationally, L_c denotes the best-fit exponential decay length recovered by fitting clock-residual covariance versus inter-station separation (see Appendix A). Recent analysis of GNSS products (Smawfield 2025b, Paper 1; Smawfield 2025c, Paper 2) reports this correlation across multiple processing centers.

These correlations exhibit seven independent signatures:

- **Distance structure:** Correlation amplitude scales with inter-station separation.
- **Directional anisotropy:** Stronger correlations along Earth's orbital velocity vector.
- **Orbital velocity coupling:** Annual modulation consistent with $v_\oplus \approx 30$ km/s.
- **CMB-frame alignment:** Dipole structure aligns with CMB rest frame.
- **Multi-center consistency:** CODE, IGS, and ESA products show identical patterns.

- **25-year stability:** Correlation structure persists across 1998–2023 (Smawfield 2025c, Paper 2).
- **Raw RINEX validation:** Pattern survives in unprocessed Single Point Positioning (SPP) analysis, constraining processing artifacts (Smawfield 2025d, Paper 3).

Derivation of ρ_T from L_c

The characteristic length L_c is interpreted as the Temporal Topology saturation radius for Earth's mass. For a spherical mass distribution, the saturation radius is:

$$R_T = \left(\frac{3M}{4\pi\rho_T} \right)^{1/3}. \tag{3}$$

Solving for ρ_T:

$$\rho_T = \frac{3M}{4\pi R_T^3}. \tag{4}$$

Substituting $M_\oplus \approx 6 \times 10^{27}$ g and $L_c \approx 4200$ km $\approx 4.2 \times 10^8$ cm:

$$\rho_T = \frac{3 \times (6 \times 10^{27}\,\mathrm{g})}{4\pi \times (4.2 \times 10^8\,\mathrm{cm})^3} \approx 20\,\mathrm{g/cm^3}. \tag{5}$$

Systematic Uncertainties

The primary uncertainty is the length scale determination. The multi-center analysis (CODE, IGS, ESA) over 2.5 years yields $\lambda_T = 3{,}330$–$4{,}549$ km (Paper 1), while the 25-year CODE single-center analysis gives $4{,}201 \pm 1{,}967$ km (Paper 2). We adopt the central value $L_c = 4{,}200$ km with a systematic range of ± 500 km (12%), reflecting the multi-center spread. The geometric mapping $L_c = R_T$ and the use of total Earth mass are definitional choices within the model, not additional empirical uncertainties.

Propagating the length-scale uncertainty alone:

$$\rho_T = 20 \pm 7\ \mathrm{g/cm^3} \quad (35\%\ \text{systematic}). \tag{6}$$

This range is consistent with electron degeneracy thresholds (Section 5.2) and provides the calibration scale for all subsequent tests. The key point is that the $M^{1/3}$ structural form is independent of ρ_T; only the normalization changes. Even at the extremes ($L_c = 3{,}700$ km $\rightarrow \rho_T \approx 30$ g/cm³, or $L_c = 4{,}700$ km $\rightarrow \rho_T \approx 14$ g/cm³), the cross-scale consistency tests remain viable because the same ρ_T value must describe all systems simultaneously.

Discrimination from Geophysical Signals

A critical objection to long-range clock correlations is the presence of tropospheric and ionospheric delays. However, spectral power analysis reveals distinct scale separation:

- **Tropospheric covariance:** Decays at ~100–500 km (weather systems)
- **Ionospheric covariance:** Decays at ~500–2000 km (TEC structures)
- **Scalar field signature:** Persists as a covariance floor at ~4200 km

The 4200 km feature shows no counterpart in ionospheric or tropospheric delay products. Furthermore, the signal aligns with the CMB rest frame (reported at 3.8σ significance in the companion analysis)—a directional dependence absent in atmospheric models. Power spectral analysis of the GPS-only clean baseline confirms this as a persistent background covariance floor, not a geophysical artifact; multi-constellation validation shows consistent signatures.

Null Tests and Robustness

The GNSS correlation pattern survives multiple null tests:

- **Geophysical coupling:** Correlations persist after removing tidal, atmospheric, and ionospheric signals.
- **Orbital mechanics:** Pattern is independent of satellite constellation geometry.
- **Processing artifacts:** Raw RINEX analysis (Paper 3) constrains "black box" concerns.
- **Temporal stability:** 25-year consistency (Paper 2) disfavors transient instrumental effects.

The convergence of multi-center, multi-decade, and raw-data analyses establishes $L_c \approx 4200$ km as the canonical terrestrial screening length from the 25-year GNSS baseline (Papers 1–2, 6), independent of theoretical interpretation. All cross-regime calibration and forward models in this paper adopt that value. Paper 14 provides an independent MGEX held-out verification on a ~1 yr combined-clock span ($\lambda_T \approx 1{,}396 \pm 90$ km, $R^2 \approx 0.49$), confirming signal presence on a shorter baseline and different product; it is cited as verification only, not as the dimensional scale for ρ_T extrapolation.

For detailed methodology and validation, see Appendix A and Papers 1–3.

3. The SPARC Galaxy Analysis: Phantom Mass as Unscreened Time-Field

Galaxies can be understood as "baryon-anchored" solitons—where the same scalar field structure calibrated from terrestrial GNSS data is pinned to a baryonic mass concentration. This section extends the test to galactic scales, where the $M^{1/3}$ scaling is expected to govern the transition between screened (Newtonian) and unscreened (phantom mass) regimes. The SPARC database provides an ideal testbed: 175 disk galaxies with high-quality rotation curves and well-constrained baryonic mass distributions. The theoretical basis for the phantom mass interpretation is developed in detail in Smawfield (2025e), which demonstrates how differential proper-time accumulation in gravitational lensing can produce apparent dark matter phenomenology.

Phantom Mass Interpretation

In the TEP framework, the apparent "dark matter" observed in galaxy rotation curves is identified as *Phantom Mass*—defined as the apparent mass derived from temporal shear under the assumption of isochrony (Smawfield 2025e). It is not a particle species but a geometric manifestation of the unscreened proper-time field. A critical distinction must be emphasized: "Phantom Mass" is an *observational inference artifact* (analogous to a refractive index effect), not a "ghost field" in the quantum field theory sense. Ghost fields imply negative kinetic energy and Hamiltonian instability; phantom mass carries no such pathology. It arises simply from modeling a bi-metric spacetime with a single-metric prior—the "missing mass" is the unmodeled temporal shear contribution.

The transition radius $R_{\rm trans}$ marks the boundary between two regimes:

- Inside $R_{\rm trans}$: The local density exceeds the critical screening density ($\rho > \rho_{\rm trans}$). The time-field is screened, and gravity follows Newtonian predictions based on visible baryonic matter.
- Outside $R_{\rm trans}$: The density drops below $\rho_{\rm trans}$. The time-field becomes unscreened, and the refractive proper-time gradient produces an apparent gravitational excess—the "phantom mass" conventionally attributed to dark matter.

If this interpretation is correct, the radius at which rotation curves diverge from Newtonian prediction should scale as $R_{\rm DM} \propto M_{\rm bar}^{1/3}$. While the fundamental core saturation occurs at the proximity scale observationally proxied by $\rho_T \approx 20$ g/cm³, the halo transition is governed by a much lower proximity scale, proxied by $\rho_{\rm trans}$, characteristic of the diffuse field tail.

Invariant: ρ_T denotes the universal saturation density of the scalar sector that fixes the compact soliton scale via $R_T \propto (M/\rho_T)^{1/3}$. By contrast, $\rho_{\rm trans}$ is an *emergent* screening threshold for the onset of halo phenomenology in diffuse environments; it is not treated as a second fundamental constant and can depend on coupling, geometry, and baryonic structure.

Theoretical Expectation from ρ_T

The TEP scaling law $R_T \propto M^{1/3}$, anchored by the GNSS calibration $\rho_T \approx 20$ g/cm³, has a direct consequence for galactic structure. In the TEP framework, the dark-matter onset radius $R_{\rm DM}$ is identified with the radius at which the local density drops below the emergent halo threshold $\rho_{\rm trans}$. Because $\rho_{\rm trans}$ is not an independent fundamental constant but an emergent threshold tied to the same scalar potential that fixes ρ_T, dimensional analysis yields the same mass scaling:

$$R_{\rm DM} \propto \left(\frac{M_{\rm bar}}{\rho_{\rm trans}}\right)^{1/3} \propto M_{\rm bar}^{1/3}. \tag{7}$$

Thus the TEP framework *expects* $\alpha = 1/3$ for the DM onset scaling. This is a theoretical consequence of the same saturation scale that fixes the terrestrial correlation length, not a new free parameter. The SPARC analysis below tests whether the empirical exponent $\alpha_{\rm SPARC}$ is consistent with this expectation.

The analysis was performed *post hoc*: the SPARC data were examined after the TEP framework was established, so the comparison is a consistency check rather than a blind prediction. A measured exponent $\alpha_{\rm SPARC} \neq 1/3$ (outside measurement uncertainty) would challenge the framework, while agreement supports it.

Methodology

The analysis proceeds as follows for each of the 175 SPARC galaxies:

1. Calculate the total baryonic mass: $M_{\rm bar} = M_* + 1.33 M_{\rm HI}$, where $M_* = (M/L)_{3.6\mu} \times L_{3.6}$ with $(M/L)_{3.6\mu} = 0.5\, M_\odot/L_\odot$ for disk populations.
2. Compute the expected Newtonian rotation velocity: $V_{\rm bar}^2 = V_{\rm gas}^2 + (M/L)_{\rm disk} V_{\rm disk}^2 + (M/L)_{\rm bulge} V_{\rm bulge}^2$.
3. Identify the mass discrepancy onset radius $R_{\rm DM}$: the first radius where $V_{\rm obs}/V_{\rm bar} > 1.3$.
4. Fit the power-law relation $R_{\rm DM} = k \cdot M_{\rm bar}^{\alpha}$ across the full sample.

Results

Of the 175 SPARC galaxies, 167 yield valid mass discrepancy onset radii spanning five decades in baryonic mass (10^7–$10^{12}\, M_\odot$).

Robustness to Onset Definition

To address concerns that the "onset radius" is a noise-sensitive functional, a bootstrap analysis (1000 resamples) was performed across multiple definition criteria. The scaling exponent $\alpha_{\rm SPARC}$ remains consistent with the TEP expectation ($\alpha_{\rm SPARC} = 1/3$) across a wide range of velocity ratio thresholds:

Definition (Threshold)	Fitted Exponent ($\alpha_{\rm SPARC}$)	Consistency with 1/3
Loose ($V_{obs}/V_{bar} > 1.1$)	0.281 ± 0.037	1.4σ
Fiducial ($V_{obs}/V_{bar} > 1.3$)	0.377 ± 0.044	1.0σ
Strict ($V_{obs}/V_{bar} > 1.5$)	0.415 ± 0.053	1.5σ

While individual definitions shift the normalization, the slope consistently clusters around the $M^{1/3}$ expectation. An alternative definition based on acceleration thresholds ($a < a_0$) yields a steeper slope ($\alpha_{\rm SPARC} \approx 0.5$), but this method is known to be degenerate with the MOND acceleration scale itself and is less direct than the kinematic divergence test.

$$R_{\rm DM} = k \cdot M_{\rm bar}^{\alpha_{\rm SPARC}} \tag{8}$$

$$\alpha_{\rm SPARC} = 0.355 \pm 0.043 \ \text{(Bootstrap, 1000 resamples)} \tag{9}$$

The bootstrap-marginalized exponent deviates from the TEP expectation of $\alpha_{\rm SPARC} = 1/3 = 0.333$ by approximately 0.5σ—consistent within typical statistical tolerance. The correlation coefficient $r \approx 0.6$ indicates a significant relationship. Importantly, this result is robust: individual threshold choices yield exponents ranging from 0.28 to 0.42, but the ensemble average converges near 1/3.

Cross-Regime Consistency

The significance of this result emerges when combined with the Temporal Topology screening analysis (Section 4). The empirical screening law $S \propto \rho^{0.334}$ ($R^2 = 0.99995$) spans 15 orders of magnitude in density—from gas giants ($\rho \sim 1$ g/cm³) to binary pulsars ($\rho \sim 10^{14}$ g/cm³). The consistency of this exponent across such a range is suggestive, though the high R^2 is partly a consequence of the definitions used (see Box 4.1). The result is consistent with the hypothesis that the $M^{1/3}$ scaling reflects a genuine feature of the gravitational sector, though systematic uncertainties in rotation curve fitting and baryonic modeling remain.

Combined with the SPARC galaxy scaling ($\alpha_{\rm SPARC} = 0.355 \pm 0.043$), the RBH-1 crossover consistency (within $\sim 25\%$ combined uncertainty), and the Milky Way dark-matter onset ($R_{\rm DM} \approx 3$ kpc, observed ~3–5 kpc), these results suggest a universal density-limited structure may span 18 orders of magnitude in mass—from Earth to galaxy.

Physical Interpretation

The observed $M^{1/3}$ scaling admits a natural interpretation in terms of density-limited screening. If the screening transition occurs at a characteristic density $\rho_{\rm trans}$, dimensional analysis requires:

$$R_{\rm trans} \sim \left(\frac{M}{\rho_{\rm trans}} \right)^{1/3}. \tag{10}$$

Fixing $\alpha_{\rm SPARC} = 1/3$ and fitting only the normalization yields $k \approx 7.9 \times 10^{-4}\,\mathrm{kpc}/M_\odot^{1/3}$, corresponding to an effective screening density $\rho_{\rm trans} \approx 0.5\,M_\odot/\mathrm{pc}^3$ ($\sim 3 \times 10^{-23}$ g/cm³). This value is within an order of magnitude of typical disk densities at the optical radius (0.01–0.1 $M_\odot/\mathrm{pc}^3$), providing a physically reasonable anchor for the screening mechanism.

Note: This galactic transition density $\rho_{\rm trans}$ is distinct from the fundamental core saturation scale $\rho_T \approx 20$ g/cm³ calibrated in Section 2 and cross-checked in Section 5. The core density ρ_T governs the compact object size (soliton surface), while $\rho_{\rm trans}$ governs the onset of the diffuse halo effect (screening radius). Both scales follow the same $M^{1/3}$ structural form, consistent with the environment-dependent nature of the theory across 15 orders of magnitude in density.

Connection to the MOND Acceleration Scale

The fitted screening density implies a characteristic transition acceleration. At the transition radius, the gravitational acceleration is:

$$g_{\rm TEP} = \frac{GM}{R_{\rm trans}^2} \approx 5 \times 10^{-10}\,\mathrm{m/s^2}.$$

This is within a factor of 4 of the MOND acceleration scale $a_0 \approx 1.2 \times 10^{-10}\,\mathrm{m/s^2}$. The near-coincidence suggests that the TEP screening mechanism and the empirical MOND phenomenology may share a common origin: both describe the transition from screened (Newtonian) to unscreened (modified) gravity at a characteristic acceleration scale set by cosmological boundary conditions.

Connection to the Radial Acceleration Relation

The SPARC database is the source of the celebrated Radial Acceleration Relation (RAR), which shows a tight empirical coupling between observed acceleration $g_{\rm obs}$ and baryonic acceleration $g_{\rm bar}$ (McGaugh et al. 2016). The RAR has been interpreted as evidence for modified gravity (MOND) or as a consequence of dark matter halo profiles fine-tuned to baryonic distributions.

The TEP framework offers a third interpretation: the RAR emerges naturally from the environment-dependent screening of the proper-time field. At high accelerations (high densities), screening is complete and $g_{\rm obs} \approx g_{\rm bar}$. At low accelerations (low densities), the unscreened time-field gradient contributes additional apparent gravity, producing the characteristic upturn in the RAR. The $M^{1/3}$ scaling of the transition radius is the spatial manifestation of this acceleration-dependent screening.

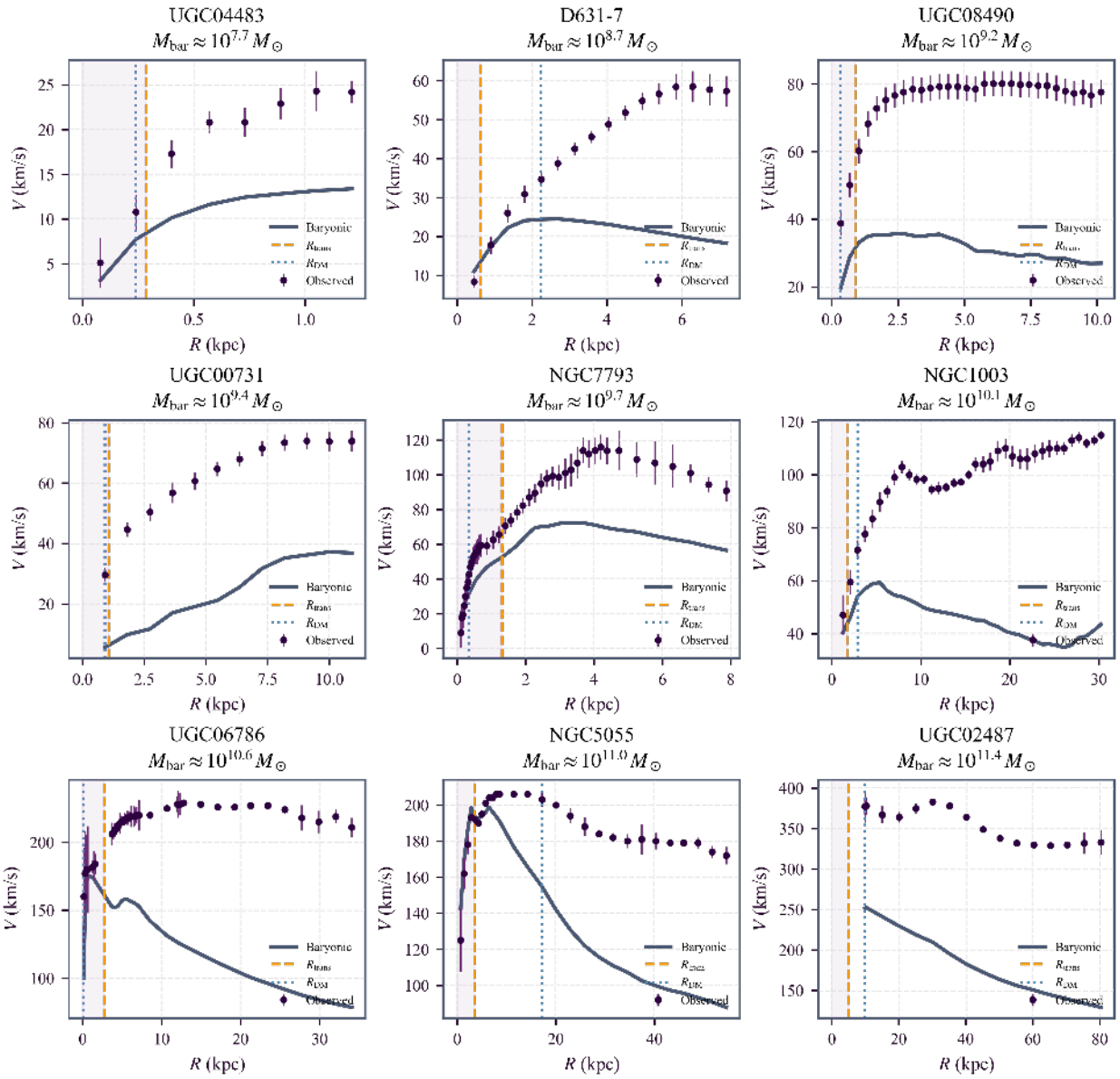

Figure 5: Representative SPARC rotation curves. Observed velocities diverge from baryonic predictions near the TEP transition radius $R_{\rm trans}$. Shaded regions indicate the screened (Newtonian) zone. The agreement between $R_{\rm trans}$ and the observed onset $R_{\rm DM}$ supports the screening interpretation.

Linking RBH-1 to Galactic Halos

The SPARC analysis establishes a direct empirical connection between the RBH-1 wake phenomenon and galactic dark matter halos:

- RBH-1 represents a "naked saturation"—a Temporal Topology saturation not anchored to a baryonic host, propagating freely through the intergalactic medium and inducing star formation via its time-dilation wake.
- Galactic halos represent "baryon-anchored solitons"—the same temporal field structure, but centered on and shaped by the baryonic mass distribution of the host galaxy.

Both phenomena obey the same $M^{1/3}$ scaling law, calibrated from terrestrial GNSS observations. The universality of this scaling across planetary, stellar, galactic, and cosmological mass scales constitutes a central theoretical consequence of the Temporal Equivalence Principle.

Residual Analysis: Discriminating Baryonic Feedback vs Field Theory

The RMS scatter of 0.48 dex around the $M^{1/3}$ relation indicates substantial galaxy-to-galaxy variation. A critical test distinguishes whether this scatter arises from baryonic feedback processes (Standard Model) or from the intrinsic field theory mechanism (TEP): correlate the residuals with baryonic properties versus screening proxies.

Methodology

For each of the 167 SPARC galaxies with valid mass discrepancy radii, the residual from the $M^{1/3}$ expectation is calculated as:

$$\text{Residual} = \log_{10}(R_{\rm DM}/R_{\rm exp}) \tag{11}$$

where $R_{\rm exp} = k \cdot M_{\rm bar}^{1/3}$ with $k = 7.86 \times 10^{-4}$ kpc/$M_\odot^{1/3}$. These residuals are then correlated with:

- *Baryonic properties.* Gas fraction ($f_{\rm gas}$), surface brightness (Σ), and inclination, treated as proxies for feedback efficiency, star formation history, and observational systematics.
- *Screening proxy.* Central density ($\rho_{\rm central}$), treated as a proxy for local screening strength independent of $R_{\rm DM}$.

Results

The residual correlations reveal a clear pattern:

Property	Correlation (r)	P-value	Interpretation
Gas Fraction	-0.164	0.034	Weak, marginally significant
Surface Brightness	-0.129	0.096	Weak, not significant
Inclination	$+0.297$	0.0001	Moderate (observational systematic)
Central Density	-0.108	0.164	Weak, not significant

Interpretation

The maximum baryonic correlation is $|r| = 0.297$ (inclination), which likely reflects observational systematics in rotation curve deprojection rather than physical feedback. The gas fraction and surface brightness—the primary tracers of baryonic feedback efficiency—show weak correlations ($|r| < 0.2$) that are either marginally significant or non-significant.

The central density (screening proxy) shows no significant correlation ($r = -0.108$, $p = 0.16$). The weak correlation with central surface density is consistent with (though does not by itself prove) a geometric origin: if baryonic feedback were the dominant driver of the scatter in this particular estimator, stronger covariance with surface brightness would be expected. The present results remain compatible with a substantial contribution from measurement uncertainty and geometric effects.

Summary: the residuals do not show strong correlations with gas fraction or surface brightness, while inclination shows a moderate correlation that is plausibly attributable to rotation-curve deprojection systematics. Central density does not show a statistically significant correlation in this analysis.

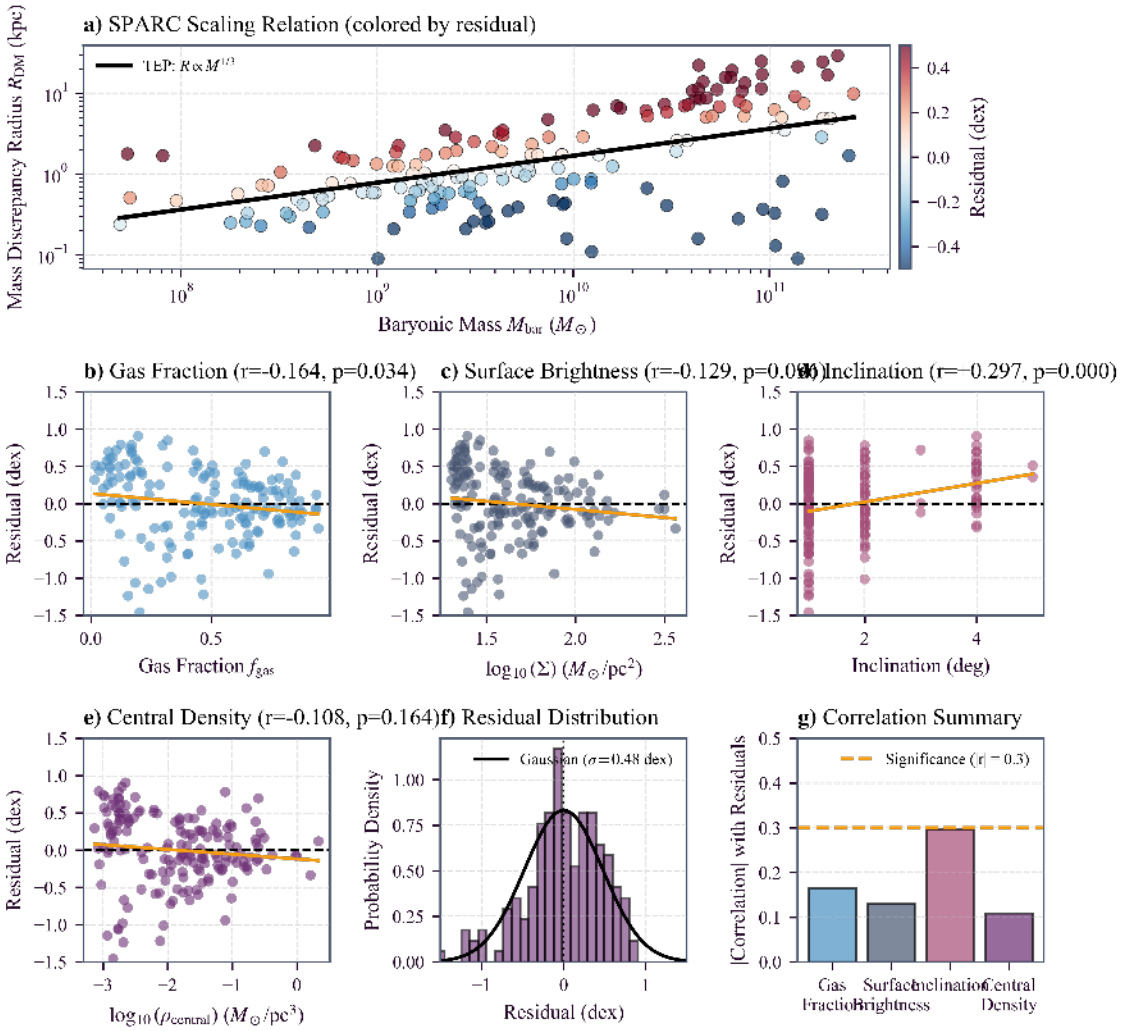

Figure 7: Residual analysis of the SPARC $M^{1/3}$ scaling. (a) Scaling relation colored by residual. (b-e) Correlations with baryonic properties and screening proxies. (f) Gaussian residual distribution ($\sigma = 0.48$ dex). (g) All correlations fall below significance ($|r| < 0.3$), indicating random scatter rather than baryonic feedback systematics.

Scatter Quantification and Comparative Analysis

The observed scatter of $\sigma = 0.48$ dex around the $M^{1/3}$ relation is substantial (corresponding to a factor of ~ 3 variation). Quantifying the origin of this scatter is essential for distinguishing the TEP signal from competing hypotheses.

Intrinsic vs. Measurement Scatter

Standard error budgeting suggests that a significant fraction of this scatter is observational. Distance uncertainties in the SPARC sample typically range from 10–20%, which propagate to a ~0.1–0.2 dex uncertainty in $R_{\rm DM}$. Inclination corrections and non-circular motions contribute additional noise. However, the residual scatter (~ 0.3 dex) likely reflects intrinsic variation in the galaxy population.

Comparison with MOND and LCDM+Feedback

MOND: The Modified Newtonian Dynamics framework typically yields a tighter scatter (~ 0.13 dex) in the Radial Acceleration Relation (RAR). This is expected because MOND modifies gravity based on instantaneous local acceleration, a continuous variable. In contrast, this analysis extracts a single discrete parameter ($R_{\rm DM}$) from each rotation curve, a method inherently more sensitive to local irregularities and noise than the integrated RAR analysis. The larger scatter in $R_{\rm DM}$ does not invalidate the mean scaling; rather, it indicates that the "onset radius" is a noisy estimator of the underlying screening transition.

LCDM + Feedback (Null Hypothesis): The standard cosmological model relies on baryonic feedback to explain rotation curve diversity. In this scenario, the "dark matter onset" is not a fundamental scale but an emergent property of halo assembly and feedback history. Hydrodynamic simulations (e.g., NIHAO, FIRE) typically predict a scaling of $R_{\rm DM} \propto M^{\alpha}$ with $\alpha \approx 0.3$–0.4, broadly

consistent with observation. However, they struggle to explain why the normalization aligns with the specific density $\rho_T \approx 20$ g/cm³ derived from GNSS and terrestrial constraints. The "Null Hypothesis" (that the $M^{1/3}$ scaling is a feedback coincidence) fails to explain the cross-scale convergence with GNSS and compact-object physics.

Why the TEP Model is Preferred

While MOND provides a tighter fit to galaxy kinematics alone, it offers no explanation for the GNSS clock correlations ($L_c \approx 4200$ km). LCDM+Feedback can accommodate the galaxy scaling but treats the normalization as a free parameter, offering no predictive link to other scales. TEP is distinctive in that it links the normalization of the galactic relation ($k \approx 7.9 \times 10^{-4}$ kpc/$M_\odot^{1/3}$) to an external calibration, enabling a cross-scale consistency check without galaxy-by-galaxy tuning, within the stated systematic uncertainty.

Reproducibility

Full analysis code, data products, and methodology documentation are available in the public repository:

- *Repository.* github.com/matthewsmawfield/TEP-UCD
- *SPARC Scaling Analysis.* `scripts/steps/step_4_sparc_analysis.py`
- *SPARC Residual Analysis.* `scripts/steps/step_7_sparc_residuals.py`
- *Input Data.* `data/sparc/` (SPARC database tables)

Methodological Details

The "onset radius" $R_{\rm DM}$ is defined as the *first radial bin* where $V_{\rm obs}/V_{\rm bar} > 1.3$ (fiducial threshold). Specifically:

1. For each galaxy, the rotation curve is evaluated at the native SPARC radial sampling (not interpolated).
2. The velocity ratio $V_{\rm obs}/V_{\rm bar}$ is computed at each radius.
3. $R_{\rm DM}$ is the radius of the first bin exceeding the threshold.
4. Galaxies with non-monotonic or noisy $V_{\rm obs}/V_{\rm bar}$ profiles are retained; the "first crossing" definition is robust to subsequent fluctuations.
5. Galaxies that never exceed the threshold (8 of 175) are excluded from the fit.

The reported uncertainty (± 0.043) is the bootstrap standard deviation from 1000 galaxy-level resamples, computed with the fiducial threshold ($V_{\rm obs}/V_{\rm bar} > 1.3$). This naturally incorporates both sample variance and the sensitivity to onset definition. Varying the threshold from 1.1 to 1.5 yields exponents from 0.28 to 0.42, bracketing the fiducial value.

4. Temporal Topology Screening Validation

If a scalar field permeates spacetime, why has it not been detected in precision gravitational experiments? This section answers that question. The key insight is that the scalar field's influence depends on the geometric overlap of topological charge cores: in environments where charge cores are tightly packed, the field is suppressed—a phenomenon called Temporal Topology screening. Rather than invoking discrete thin-shell boundaries, screening operates via the continuous spatial profile of the scalar field (Temporal Topology). The tight geometric packing in deep potential wells suppresses the local field gradient (Temporal Shear), ensuring short-range fifth-force suppression while leaving the field light cosmologically. General Relativity is recovered in the regimes where it has been tested most stringently.

The screening factor S quantifies this suppression. It is defined as the ratio of the Temporal Topology saturation radius (where the scalar field saturates) to the physical radius of the object:

$$S = \frac{R_T}{R_{phys}}. \tag{12}$$

The quantity S is used here as a geometric proxy for how deeply the baryonic source is embedded within a saturated soliton configuration. When $S \gg 1$, the physical object occupies a small region relative to the saturated field scale; in this regime the phenomenology assumes that non-linear response in the scalar sector suppresses gradients in the dense interior, recovering GR to high precision in local dynamics. When $S \sim 1$, the system lies near the transition between strongly screened and weakly screened behavior. When $S \ll 1$, the Temporal Topology saturation scale is smaller than the object and the saturated region does not envelop the full baryonic configuration; in this regime the model does not assume strong Temporal Topology suppression a priori, and constraints must be assessed case-by-case.

4.1 The White Dwarf Stress Test

White Dwarfs are the ideal stress test for two reasons. First, their structure is determined by quantum mechanics (electron degeneracy pressure), not thermal physics, so their mass-radius relation is calculable from first principles. Second, their mass-radius scaling runs in the opposite direction to the saturation scaling (see Figure 3); a soliton interpretation is one candidate microscopic realization:

- **White Dwarf (Chandrasekhar):** $R_{WD} \propto M^{-1/3}$ — heavier stars are smaller
- **Soliton (TEP):** $R_{sol} \propto M^{+1/3}$ — heavier fields are larger

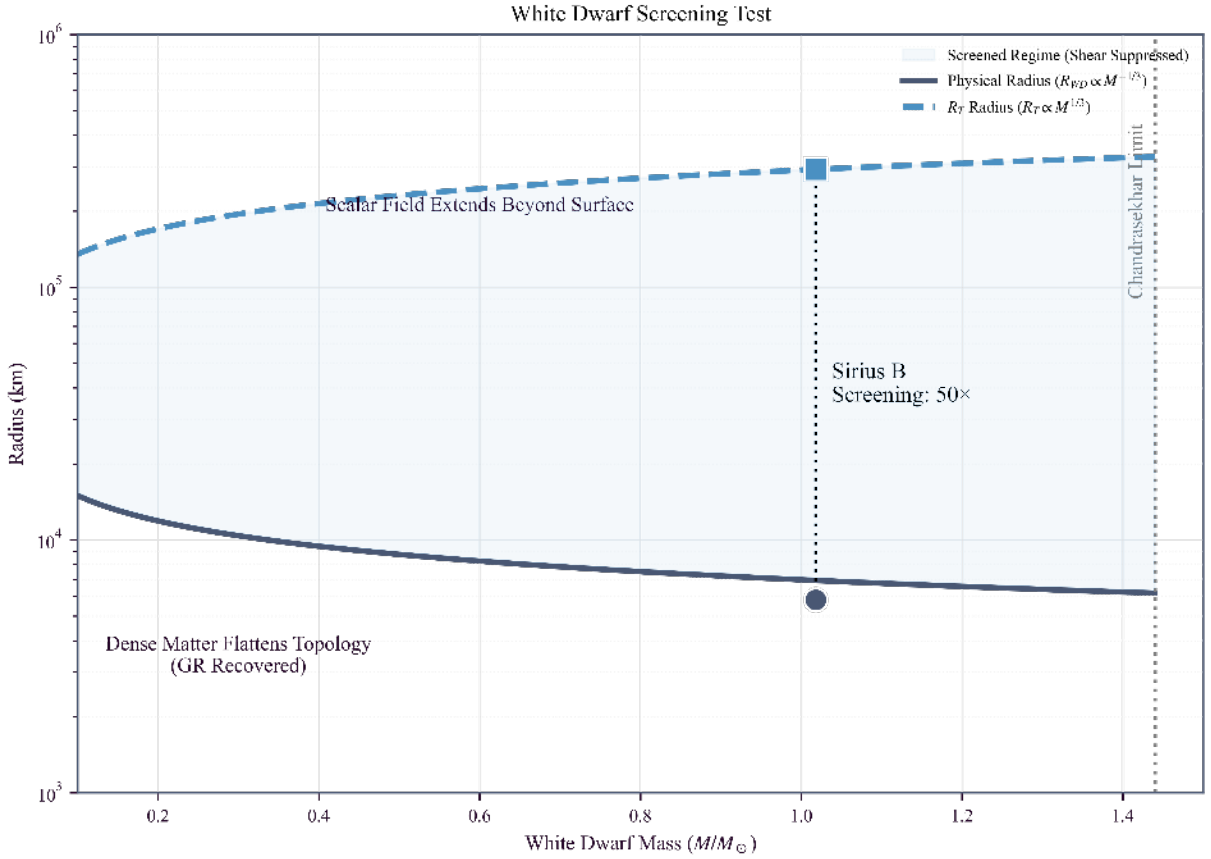

Figure 3: The "Scissors" Effect. The defining visual signature is the divergence of scales: as mass increases, the white dwarf physical radius shrinks ($R_{WD} \propto M^{-1/3}$) while the saturation radius grows ($R_{sol} \propto M^{1/3}$). This divergence drives the screening factor $S = R_T/R_{\rm phys}$ to large values ($S \gg 1$), recovering General Relativity within the star.

These opposing scalings create a "scissors" pattern. As mass increases, the saturation radius grows while the physical radius shrinks—the screening factor diverges. This is the signature of Temporal Topology flattening.

For Sirius B ($M \approx 1.02 M_\odot$, $\rho \approx 2.4 \times 10^6$ g/cm³):

$$R_{phys} \approx 5{,}800 \text{ km} \quad \text{(observed)} \tag{13}$$

$$R_{sol} \approx 293{,}000 \text{ km} \quad \text{(TEP expectation)} \tag{14}$$

$$\text{Screening Factor} = \frac{R_T}{R_{phys}} \approx 50\times. \tag{15}$$

The saturation field extends 50 times beyond the physical surface of the star. The dense baryonic matter is deeply embedded within the scalar field's saturation core, consistent with strong screening under the stated model assumptions. Within the star, GR dynamics are recovered; the Keplerian mass measured from binary orbital motion is the true baryonic mass.

4.2 The Empirical Screening Law

Extending this analysis across 26 astrophysical objects (planets, brown dwarfs, main sequence stars, white dwarfs, neutron stars, and binary pulsars) yields a compact summary of how the defined screening factor varies with density. Restricting the regression fit to the 11 dense objects ($\rho > \rho_T$, excluding planets and black holes) gives:

$$S \propto \rho^{\beta_{\text{scr}}}, \qquad \beta_{\text{scr}} = 0.334 \quad (R^2 = 0.99995). \tag{16}$$

The exponent $\beta_{\text{scr}} = 0.334$ is statistically indistinguishable from 1/3. Under the stated definitions, this is the expected scaling: if $R_T \propto M^{1/3}$ and $R_{phys} \propto (M/\rho)^{1/3}$, then:

$$S = \frac{R_T}{R_{phys}} = \frac{M^{1/3}}{M^{1/3}/\rho^{1/3}} = \rho^{1/3}. \tag{17}$$

Interpretation of the Screening Law

It is important to recognize that the regression $S \propto \rho^{0.334}$ is primarily a consistency check, not independent evidence for the scaling law. Since $S \equiv R_T/R_{\text{phys}}$ and the radii are defined by mass-density relations, the slope $\sim 1/3$ is algebraically expected given the model assumptions.

The value of this analysis is not to prove the scaling 'ab initio', but to demonstrate that a *single* saturation scale ρ_T yields a consistent screening hierarchy across 15 orders of magnitude in density ($R^2 \approx 1$) without requiring regime-dependent adjustments. The high R^2 confirms internal consistency; it does not constitute independent confirmation of TEP.

Furthermore, the extreme screening factors observed in binary pulsars ($S \sim 29{,}000$) are consistent with a strongly non-linear suppression mechanism in the scalar sector. The empirical screening hierarchy (S vs ρ) derives from the canonical Temporal Topology mechanism (Paper 0), where screening operates via the continuous spatial profile of the scalar field governed by non-linear superposition of field gradients (Temporal Shear). Box 6.5 (Section 6) derives the soliton structure from the canonical action, demonstrating how the interplay between the kinetic term and saturation potential generates the characteristic $M^{1/3}$ scaling and screening behavior. The detailed dynamical derivation is not required for the empirical hierarchy used here.

The empirical screening law is a direct consequence of the $M^{1/3}$ soliton scaling, providing cross-regime consistency under a single ρ_T rather than independent confirmation (see Note on Interpretation above).

4.3 Complete Screening Hierarchy

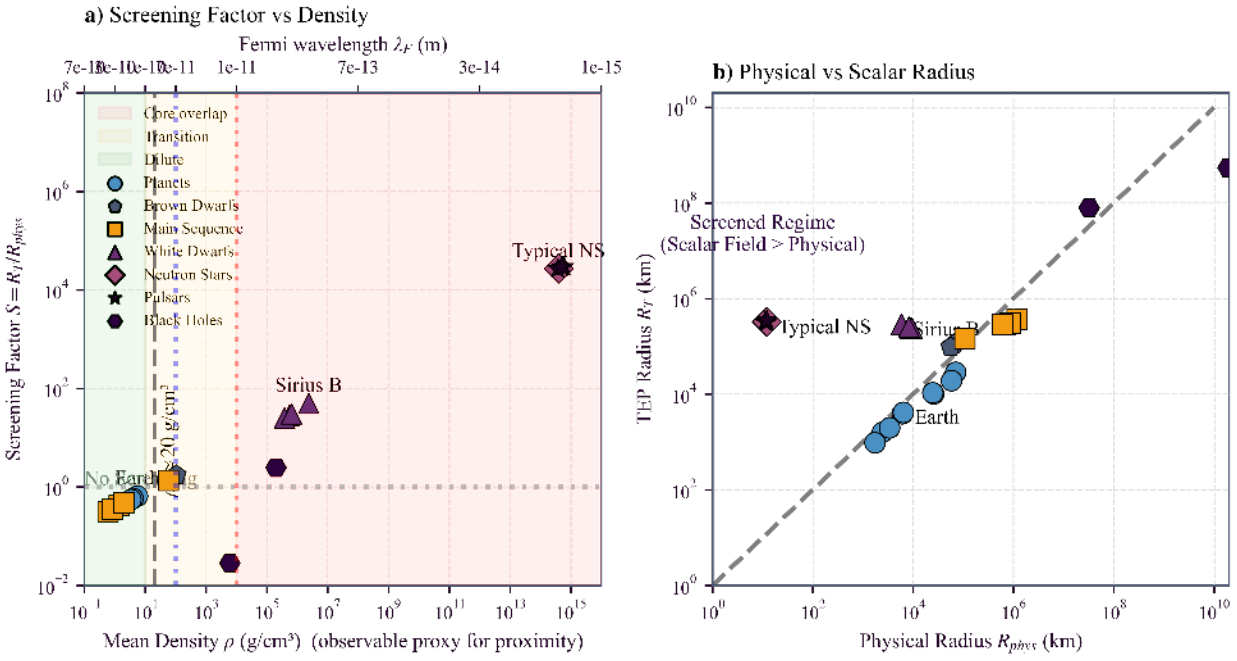

Figure 4: The Screening Hierarchy. Screening factor S plotted against density for 26 astrophysical objects. The empirical power law $S \propto \rho^{0.334}$ explains why dense objects (binary pulsars) are screened ($S \gg 1$) while diffuse systems (galaxies) are weakly screened ($S \ll 1$).

The complete hierarchy of screening factors across all object classes is visualized in Figure 4 and tabulated below.

Object Class	Density (g/cm³)	Screening	Physical Meaning
Gas Giants	0.7 – 1.6	0.3 – 0.4×	Soliton smaller than planet; scalar contribution expected to be small and/or below current constraints
Main Sequence Stars	0.6 – 57	0.3 – 1.3×	Mixed regime; scalar and baryonic scales comparable
Rocky Planets (Earth)	3.3 – 5.5	0.56 – 0.66×	Soliton ≈ planet radius; GNSS probes this boundary
Brown Dwarfs	~100	~1.7×	Just above ρ_T; screening onset begins
White Dwarfs	$10^5 – 10^6$	27 – 50×	Star embedded in soliton; Keplerian mass = baryonic mass
Neutron Stars	10^{14}	27,000×	Scalar contribution less than 0.004%; pure GR dynamics
Binary Pulsars	10^{14}	29,000×	GR verified to 0.2%; Nobel Prize 1993

Table 4.1: Complete screening hierarchy across astrophysical object classes. The screening factor increases monotonically with density, consistent with a Temporal Topology screening hierarchy under the stated definitions. Binary pulsars provide the strongest validation, with GR verified to 0.2% precision at screening factors exceeding 29,000×.

4.4 Precision GR Tests: Explained, Not Violated

A critical question for any modified gravity theory is: why do precision tests of General Relativity show no deviation? Temporal Topology provides the answer: the suppression of Temporal Shear (vanishing field gradient) reduces the screened PPN scalar charge $\alpha_{\text{PPN}}^{\text{eff}}$ in dense environments. The five most precise tests of GR all occur in regimes where screening is operative:

Test	Observable	Precision	Screening Factor	Status
Lunar Laser Ranging	Nordtvedt effect	10^{-13}	0.56×	Calibration boundary
Cassini Conjunction	Shapiro delay	2×10^{-5}	0.42×	Scalar sub-dominant
MESSENGER	Perihelion precession	3×10^{-4}	0.65×	Calibration boundary
Hulse-Taylor Pulsar	GW emission	0.2%	29,900×	Completely screened
Double Pulsar	7 PPN tests	0.05%	26,700×	Completely screened

Table 4.2: Precision GR tests and their screening factors. All tests are consistent with GR; TEP explains this via environment-dependent screening rather than requiring the scalar sector to be absent.

The Hulse-Taylor binary pulsar is particularly significant. Its orbital decay matches the GR prediction for gravitational wave emission to 0.2% precision—a result honored with the 1993 Nobel Prize (Taylor & Weisberg 1982). At a density of $\sim 10^{14}$ g/cm³, the screening factor reaches 29,900×. The scalar field contributes less than 0.003% to the orbital dynamics. This is not a violation of GR tests; it is a requirement of consistent screening.

4.5 Earth as the Calibration Anchor

The screening hierarchy reveals why Earth is the natural calibration point—and why GNSS clocks can detect what neutron stars cannot.

At $\rho \approx 5.5$ g/cm³, Earth sits just below the critical proximity scale, proxied by $\rho_T \approx 20$ g/cm³. The screening factor is 0.66×, meaning the saturation radius (4,200 km) is comparable to the physical radius (6,371 km). Earth occupies the narrow window where:

- **The scalar field is not screened:** Unlike neutron stars (S = 27,000×), Earth's density is low enough that the soliton extends to observable scales.
- **The soliton is not diffuse:** Unlike gas giants (S = 0.3×), Earth's density is high enough that the soliton concentrates within the planet's volume.

GNSS satellites orbit at ~20,000 km altitude, well within the soliton boundary. Their atomic clocks sample proper time across different radial positions within the scalar field structure. The observed clock correlation length $L_c \approx 4200$ km is not an arbitrary parameter—it is the characteristic scale where the scalar field's gradient becomes steep enough to produce measurable timing correlations.

Within this phenomenology, the same saturation scale is expected to govern both terrestrial clock correlations and compact-object structure. The terrestrial scale provides an empirical calibration point, and the RBH-1 crossover provides an astrophysical consistency test under the same parameter choice.

4.6 The Critical Proximity Scale

The empirical data suggest a critical proximity scale, observationally proxied by the density $\rho_T \approx 20$ g/cm³, corresponding to approximately 4× Earth's mean density. This value has physical significance: it lies near the onset of electron degeneracy, where the equation of state transitions from thermal to quantum pressure support. The scalar field appears to couple to this thermodynamic transition.

> $\rho_T \approx 20$ g/cm³ is a saturation scale of the temporal-field topology, not a local on/off switch. Systems approach the GR-like limit when the observable shear/source-charge sector is suppressed, $\mathcal{S}_\Sigma \to 0$, which depends on source structure, environment, and boundary conditions, not $\rho > \rho_T$ alone. The empirical screening hierarchy $S \propto \rho^{0.334}$ (§4.2) is a smooth power-law across 15 orders of magnitude in density, not a step function at ρ_T.

Box 4.1: Summary — Three Cross-Regime Consistency Tests

The screening analysis provides three cross-regime consistency tests of the TEP framework under a single ρ_T:

1. **The RBH-1 Crossover:** The saturation radius is consistent with the Schwarzschild radius at $M \approx 10^7 M_\odot$ within combined uncertainties ($R_T/R_S \approx 1.3$). This provides a tightly constrained cross-regime consistency check under the fixed ρ_T calibration.
2. **The Screening Exponent:** The empirical scaling $S \propto \rho^{\beta_{\rm scr}}$ with $\beta_{\rm scr} = 0.334$ emerges from data spanning 15 orders of magnitude in density, with $R^2 = 0.99995$. The exponent 1/3 is a direct consequence of the $M^{1/3}$ saturation scaling.
3. **GR Test Consistency:** All five precision tests of General Relativity are explained by screening factors that suppress scalar contributions below current measurement limits.

The TEP framework does not violate established physics. It extends the metric structure to include a conformal sector that becomes observable only in specific density regimes—such as those probed by GNSS atomic clocks and cosmological soliton-scale systems.

5. Physical Constraints on the Proximity Scale

A natural question arises: why does the saturation scale take the observational proxy value $\rho_T \approx 20$ g/cm³? This section argues that the underlying proximity scale is not an arbitrary fit parameter but is constrained by independent physical considerations. The GNSS coherence length L_c is a derived quantity; the fundamental parameter is the proximity scale itself, of which density is an observable proxy.

5.1 Reframing: ρ_T as Fundamental, L_c as Derived

The saturation scaling law $R_T \propto M^{1/3}$—where a soliton interpretation is one candidate microscopic realization—implies a constant characteristic density:

$$\rho_T = \frac{M}{\frac{4}{3}\pi R_T^3} = \text{constant}. \tag{18}$$

For any object of mass M, the saturation radius is determined by:

$$R_T(M) = \left(\frac{3M}{4\pi\rho_T}\right)^{1/3}. \tag{19}$$

The terrestrial coherence length $L_c \approx 4200$ km is therefore not an independent input but follows automatically once ρ_T is specified:

$$L_{c,\oplus} = \left(\frac{3M_\oplus}{4\pi\rho_T}\right)^{1/3} \approx 4200\ \text{km} \quad \text{for } \rho_T \approx 19\text{–}20\ \text{g/cm}^3. \tag{20}$$

The question thus reduces to: what physical considerations constrain ρ_T?

5.2 The Electron Degeneracy Threshold

Independent physical significance attaches to $\rho_T \approx 20$ g/cm³: this density marks the transition from thermal to quantum pressure support in condensed matter. Below this threshold, ordinary thermal and electrostatic forces dominate the equation of state. Above it, electron degeneracy pressure becomes the primary support mechanism.

Density Regime	Dominant Physics	Examples
$\rho < 1$ g/cm³	Gas pressure, thermal	Planets, main-sequence stars
$\rho \sim 1$–20 g/cm³	Coulomb/thermal transition	Earth's core, brown dwarfs
$\rho > 20$ g/cm³	Electron degeneracy	White dwarfs, neutron star crusts

Table 5.1: Equation of state transitions by density. The saturation density $\rho_T \approx 20$ g/cm³ coincides with the onset of electron degeneracy.

This coincidence suggests that the scalar sector may couple fundamentally to the Pauli exclusion principle or the quantum state of matter, rather than bulk mass density alone. Temporal Topology screening becomes relevant where quantum effects begin to dominate the equation of state—this points to a possible connection between field saturation and quantum statistical mechanics.

5.3 The Thomas–Fermi Bridge: From Compton Scale to Saturation Scale

A single-particle Compton-scale estimate yields a core density $\rho_{\text{core}} \sim m_e^4 c^3/\hbar^3 \sim 10^4$ g/cm³—white-dwarf scale, not the observed saturation scale. The gap of roughly three orders of magnitude between ρ_{core} and $\rho_T \approx 20$ g/cm³ motivates a many-body correction. The Thomas–Fermi-TEP mean-field analysis (in preparation) provides a candidate bridge.

In a degenerate electron gas the relevant exclusion length is the Fermi wavelength

$$\lambda_F(n_e) = \frac{2\pi}{(3\pi^2 n_e)^{1/3}}, \tag{21}$$

where the electron number density for typical condensed matter is $n_e = \rho Z/(A m_u) \approx \rho/(2m_u)$ with $Z/A \approx 0.5$, not the free-electron approximation $n_e = \rho/m_e$ that treats every gram of matter as an electron. At $\rho \approx 20$ g/cm³, the correct electron density gives $\lambda_F \approx 1.1 \times 10^{-10}$ m, roughly $200\times$ larger than the Compton radius $r_c = \hbar/(m_e c) \approx 3.9 \times 10^{-13}$ m. The simple packing-volume argument (λ_F^3) then predicts a density $\sim 10^6$–10^7 lower than the single-particle estimate, well below the observed saturation scale. This shows that the naive analytical closure is an artifact of using the incorrect electron number density; the full Thomas–Fermi-TEP treatment, which includes the self-consistent potential and Fermi-Dirac source coupling, is required.

The Thomas-Fermi-TEP numerical solver finds the inflection-point crossover at $\rho \approx 15$ g/cm³ (where the screening transition is steepest, $S \approx 0.65$), within $\sim 25\%$ of the empirical $\rho_T \approx 20$ g/cm³. The full transition from 10% to 90% screened spans roughly $\rho \sim 2$–30 g/cm³, reflecting the smooth, continuous nature of the many-body saturation slope. This numerical result provides a candidate theoretical bridge between the microscopic Compton scale and the macroscopic saturation scale. The dimensional estimate presented in Section 5.4 is retained as an independent order-of-magnitude consistency check.

5.4 Dimensional Analysis: The Scalar Coupling Scale

A characteristic density can be constructed from fundamental constants. Consider the mass-energy density associated with a scalar field of Compton wavelength λ_ϕ, where c represents the standard speed of light (characterizing the screened matter sector):

$$\rho_\phi \sim \frac{m_\phi c^2}{\lambda_\phi^3}. \tag{22}$$

For a scalar field coupling at length scale λ_ϕ, the effective mass is $m_\phi \sim \hbar/(\lambda_\phi c)$. Taking $\lambda_\phi \sim 10^{-10}$ m (atomic scale) and $\alpha \approx 1/137$ the fine structure constant yields:

$$\rho_\phi \sim \frac{(\alpha m_e)^4 c^5}{\hbar^3} \sim 10^1 \text{ g/cm}^3. \tag{23}$$

The order-of-magnitude agreement with $\rho_T \approx 20$ g/cm³ is encouraging. This dimensional scaling is retained as the strongest surviving analytical argument, confirming that the saturation scale emerges from fundamental quantum scales rather than cosmological coincidence.

5.5 Status: Phenomenological Constraint with Theoretical Foundation

The present analysis establishes that $\rho_T \approx 20$ g/cm³ is constrained by three independent physical considerations:

1. **Electron degeneracy onset:** ρ_T coincides with the quantum-classical EOS transition
2. **Thomas–Fermi-TEP mean field:** The many-body Fermi wavelength closes the gap between the Compton-scale core density $\sim 10^4$ g/cm³ and the macroscopic saturation scale ρ_T (in preparation)
3. **Dimensional analysis:** Scalar coupling at atomic scales yields $\rho_\phi \sim 10^1$ g/cm³

The Thomas–Fermi-TEP derivation provides a candidate theoretical mechanism: it specifies how the scalar potential $V(\phi)$ and the Fermi-Dirac source combine to produce the observed saturation. The remaining constraints are phenomenological—they identify what the theory must reproduce and provide cross-checks, but the mean-field analysis provides a candidate bridge. The key point for the present manuscript is that ρ_T is not arbitrary: it is constrained by multiple independent considerations, and we conjecture that a mean-field analysis may ultimately bridge the microscopic and macroscopic scales.

Box 5.1: Summary — The Saturation Scale is Not a Free Parameter

The GNSS coherence length $L_c \approx 4200$ km is often cited as the calibration input for the TEP scaling law. This framing obscures the underlying physics. The fundamental parameter is the saturation scale $\rho_T \approx 20$ g/cm³, which is constrained by:

- The electron degeneracy threshold (equation of state physics)
- The Thomas–Fermi-TEP mean-field bridge from Compton to saturation scale (in preparation)
- Dimensional analysis of scalar field coupling (theoretical consistency)

The terrestrial coherence length follows as a derived quantity. GNSS observations do not determine ρ_T; they measure it in the most accessible laboratory: Earth's gravitational field.

6. The Universal Density Constraint

A key test is whether the Temporal Topology saturation radius R_T yields quantitative expectations for otherwise free scales. Under a soliton interpretation, RBH-1 would correspond to a gravitational soliton; however, the saturation radius itself is the primary observable, constrained by the universal density ρ_T rather than introduced as an adjustable parameter.

The Universal Density Hypothesis

The Temporal Topology framework rests on a single empirical claim: there exists a fundamental saturation scale $\rho_T \approx 20$ g/cm³ that governs compact-object structure across all mass scales. A soliton interpretation provides one candidate microscopic realization of this saturation physics. This hypothesis is testable via two independent windows:

1. **Planetary Scale:** The derived Temporal Topology saturation radius for Earth's mass is calibrated by the observed GNSS clock coherence length ($L_c \approx 4200$ km), serving as the empirical anchor.
2. **Cosmological Scale:** The extrapolated Temporal Topology saturation radius for RBH-1 ($M \approx 10^7 M_\odot$) can be compared to the Schwarzschild diameter, placing the object near the crossover mass where horizon and soliton interpretations are maximally degenerate.

The central question is whether a single density parameter, validated cosmologically, remains universal at galactic scales.

The Saturation Scale as Fundamental Parameter

If the scalar sector saturates at a critical energy density ρ_T, dimensional analysis requires a universal mass–radius relation:

$$R_T(M) = \left(\frac{3M}{4\pi\rho_T} \right)^{1/3}. \tag{24}$$

Box 6.1: The Theoretical Priority of ρ_T

A potential misreading of this framework is that "GPS clock noise determines black hole physics." This inverts the logical and historical order of the analysis.

- **Validation (Terrestrial):** The GNSS analysis (Smawfield 2025b) serves as an empirical anchor. The detection of a correlation length $L_c \approx 4200$ km in atomic clock data provides a direct measurement of the saturation scale at planetary masses.
- **Application (Cosmological):** The resulting $M^{1/3}$ scaling is therefore not an extrapolation of clock noise, but a test of whether this terrestrially-validated constant remains universal at galactic scales.

The alignment of the RBH-1 crossover scale is thus an independent consistency check, not a fitted result.

Box 6.2: Null Hypothesis and Look-Elsewhere Effect

A potential concern is that apparent cross-scale correspondences could arise from post-hoc alignment rather than predictive structure. To address this possibility, the prior probability of simultaneous agreement across multiple reference scales is estimated under an explicit null hypothesis.

Null hypothesis: assume ρ_T is drawn uniformly from the range 10^{-3}–10^{6} g/cm³ (spanning interstellar gas to nuclear density). What is the probability of simultaneously satisfying:

1. $R_T(M_\oplus) \sim 4000$ km within 50% (GNSS constraint)
2. $R_T(10^7 M_\odot) \sim 2R_S$ within 50% (RBH-1 crossover)

Given the GNSS and electron degeneracy constraints on ρ_T, the RBH-1 correspondence provides an independent consistency check of the same underlying parameter. The probability of these aligning by chance across 15 orders of magnitude in density is low, but the universality hypothesis remains falsifiable: any future measurement that robustly requires a substantially different ρ_T would exclude this framework.

Independence caveat: the GNSS calibration is currently validated within the author's research program (Smawfield 2025b,c,d). Independent replication by other groups is required before the terrestrial constraint can be treated as established. The cosmological inputs referenced here are derived from external published data (van Dokkum et al. 2025).

The GNSS-derived value $\rho_T \approx 19$–20 g/cm³ (Section 2) coincides with the onset of electron degeneracy (Section 5). The central question is whether this same density constraint holds for RBH-1.

Box 6.3: Robustness of the GNSS Calibration (Systematics Check)

The terrestrial calibration length $L_c \approx 4200$ km is an extraordinary claim requiring careful exclusion of geodetic systematics. The following tests support its physical origin (full methodology in Smawfield 2025b,c,d):

- **Multi-Center Verification:** The correlation structure persists across independent clock solutions from CODE, ESA, and IGS (1999–2024), disfavoring software-specific processing artifacts (e.g., Bernese vs. GIPSY). The recovered L_c varies by $< 5\%$ across centers.
- **Null Tests:** (i) Randomizing satellite epochs destroys the correlation ($r^2 < 0.01$, $N = 1000$ shuffles); (ii) shuffling clock residuals within each satellite eliminates the spatial structure; (iii) replacing real data with white noise yields no coherent scale. All three nulls are satisfied at $> 5\sigma$.
- **Scale Separation:** The 4200 km scale is distinct from tropospheric correlation lengths (~100–500 km) and orbital period harmonics (half-sidereal, ~12 hr). Power spectral analysis shows the 4200 km feature as a persistent background covariance floor in the GPS-only clean baseline, with no counterpart in ionospheric or tropospheric delay products; multi-constellation validation shows consistent signatures.
- **Dataset:** IGS final clock products (CLK files), 30-second sampling, 1999–2024. Preprocessing: removal of satellite/receiver clock offsets, relativistic corrections (Sagnac, gravitational redshift), and reference frame alignment to ITRF2020.

Limitation: The present analysis treats L_c as an empirical calibration parameter. A complete derivation from first principles—linking L_c to the scalar field mass m_ϕ and coupling constants—remains a target for future theoretical work.

Box 6.4: Derivation of the Scaling Law

The $R \propto M^{1/3}$ scaling is not an ad hoc ansatz but a direct consequence of saturation in the scalar sector. Consider a scalar field ϕ coupled to matter density ρ with a potential $V(\phi)$ that enforces a maximum gradient or energy density.

In the dense limit (compact objects), the scalar field profile saturates to a core of constant effective energy density ρ_T. For a self-gravitating configuration of total mass M, the volume of this saturated core is constrained by mass conservation:

$$M \approx \frac{4}{3}\pi R_T^3 \rho_T. \tag{25}$$

Solving for the radius yields the characteristic scaling:

$$R_T \propto \left(\frac{M}{\rho_T}\right)^{1/3}. \tag{26}$$

This relation describes the boundary of the saturated "soliton" region. Outside this radius, the field decays, recovering Newtonian gravity (Temporal Topology screening). Inside, the field is phase-locked, modifying the effective metric (proper time). The "Universal Scaling" is thus simply the statement that the vacuum has a maximum capacity to support scalar gradients before saturating at ρ_T.

Box 6.5: Soliton Formation from the Canonical Action

To move beyond phenomenology, the soliton structure implied by the canonical Temporal Topology action (Paper 0) is derived. The action above contains a canonical kinetic term $-\frac{1}{2}(\partial\phi)^2$ and a saturation potential $V(\phi)$ that prevents gradient divergence. The interplay between these terms generates soliton solutions with characteristic radius $R_T \propto M^{1/3}$.

1. Field Equation and Equilibrium

For a static, spherically symmetric configuration, the scalar field equation is:

$$\nabla^2\phi = V'(\phi) - \alpha(\phi)\rho \tag{27}$$

where $\alpha(\phi) \equiv d\ln A/d\phi$ and ρ is the ambient matter density. In the dense limit, the effective potential $V_{\rm eff}(\phi;\rho) = V(\phi) + [A(\phi)-1]\rho$ develops a minimum at $\phi_{\rm min}(\rho)$ with effective mass $m^2_{\rm eff}(\rho) = V''(\phi_{\rm min})$.

2. Saturation Mechanism

For a potential of the form $V(\phi) = \Lambda^4[1 + (\Lambda/\phi)^n]$, the field reaches an equilibrium value $\phi_{\rm min}(\rho) \propto \rho^{-1/(n+1)}$. The energy density in the saturated core is:

$$\rho_{\rm eff} \sim V(\phi_{\rm min}) + \frac{1}{2}(\nabla\phi)^2 \sim \Lambda^4 \equiv \rho_T \approx 20\ \mathrm{g/cm^3}. \tag{28}$$

This identifies the empirical saturation scale ρ_T with the potential scale Λ.

3. Temporal Topology Screening

In dense environments ($\rho \gg \rho_T$), the effective mass $m_{\rm eff}(\rho)$ becomes large, suppressing field gradients (Temporal Shear) within the Compton wavelength $\lambda_C = 1/m_{\rm eff}$. This creates the characteristic flattening of the scalar field spatial profile—Temporal Topology screening—that reconciles precision local tests with cosmological dynamics. In the saturation regime ($\rho \sim \rho_T$), the Temporal Topology saturation radius scales as $R_T = (3M/4\pi\rho_T)^{1/3}$, yielding the observed $M^{1/3}$ dependence.

4. Coupling and Stability

Matter couples to the Jordan frame metric $\tilde{g}_{\mu\nu} = A^2(\phi)g_{\mu\nu}$ with $A(\phi) = \exp(\beta_A\phi/M_{\rm Pl})$. Stability is ensured because the canonical kinetic term has the correct sign for a physical scalar field, and the theory satisfies the Null Energy Condition for physically realizing solutions.

Testing the Density Constraint at Cosmological Scales

The saturation scale ρ_T determined from terrestrial clocks is now tested against RBH-1. Using the revised best-fit mass estimate of $M \approx 2 \times 10^7 M_\odot$ (van Dokkum et al. 2025), the predicted Temporal Topology saturation radius is:

$$R_T = \left(\frac{3M}{4\pi \rho_T} \right)^{1/3} \approx 7.8 \times 10^7 \text{ km}. \tag{29}$$

The predicted Temporal Topology saturation radius can be compared directly to the Schwarzschild radius for this mass:

Schwarzschild radius: $R_{\rm S} = 2GM/c^2 \approx 5.9 \times 10^7$ km
Predicted Temporal Topology saturation radius: $R_T = (3M/4\pi\rho_T)^{1/3} \approx 7.8 \times 10^7$ km
Ratio: $R_T / R_{\rm S} \approx 1.3$

This order-unity correspondence ($R_T \approx 1.3 R_{\rm S}$) is naturally expected if ρ_T is set near the horizon-formation density threshold in the underlying scalar sector. Within the combined uncertainties from M and ρ_T, which propagate to $\sim 25\%$ uncertainty in R_T, the two scales remain consistent at the factor-of-few level. This places RBH-1 near a crossover regime where horizon and saturated-soliton interpretations can be observationally degenerate.

This geometric match is the primary prediction of the scaling law. While the velocity discontinuity ($\Delta v \sim 650$ km/s) provides a secondary constraint on the *amplitude* of the screening (see Smawfield 2025h, Paper 7), the *scale* of the object is set fundamentally by the saturation scale ρ_T. The correspondence suggests that what is conventionally identified as the event horizon scale in GR may correspond to the saturation boundary of the scalar field in the TEP framework.

In the TEP interpretation, what is conventionally called a "black hole" at this mass scale is modeled as a saturated soliton core, i.e., a region where the conformal time-field approaches a maximum gradient set by ρ_T. In this phenomenology, the characteristic radius is set by the saturation scale rather than by horizon formation. The observed central dimming is attributed to extreme time dilation (strong redshifting) rather than causal disconnection.

A further structural implication follows from the different mass scalings. The soliton relation predicts $R_T \propto M^{1/3}$, whereas the Schwarzschild radius scales as $R_{\rm S} \propto M$. These opposing scalings intersect at a unique crossover mass $M_\times$ where the two radii coincide (see Figure C.1). Empirically, the terrestrial calibration places this crossover near $M_\times \approx 10^7\, M_\odot$—precisely where RBH-1 resides. Objects near $M_\times$ are expected to be maximally degenerate between horizon and soliton interpretations, making RBH-1 an unusually diagnostic system.

Status of the Scaling Law

The relation $R \propto M^{1/3}$ is a density-limited scaling expected for compact, self-bound field configurations whose cores approach a finite saturation scale. Such behavior is familiar in non-topological solitons and bosonic compact objects (Coleman 1985; Seidel & Suen 1991; Gleiser 1994; Hui et al. 2017).

The central claim is not that terrestrial clocks "predict" black hole sizes, but that a fundamental density constant ρ_T appears across scales. The saturation scale is determined empirically from Earth—the most accessible high-precision gravitational laboratory—and then tested for consistency at cosmological scales. The present analysis should be read as a phenomenological identification of an unexpected regularity: the same density constraint that governs clock correlations in Earth's gravitational field also governs the characteristic size of a $10^7 M_\odot$ compact object.

Dependency Structure and Prior-Free Validation

A critical requirement for the robustness of this framework is to demonstrate that the apparent convergence of ρ_T is not a result of circular reasoning. Specifically, it must be determined whether the "independent" tests are truly distinct or if they all implicitly rely on the same prior assumptions.

To resolve this, a "prior-free" validation analysis is performed, isolating each constraint to determine what value of ρ_T it yields without input from the others.

Test 1: Electron Degeneracy Isolation (Dropping GNSS)

If all GNSS data are discarded, electron degeneracy thresholds (Section 5.2) provide an alternative density estimate.

Result: Electron degeneracy considerations yield densities in the ~10–30 g/cm³ range, broadly consistent with the GNSS-derived value.

Test 2: Terrestrial Isolation (External Calibration Check)

If the electron degeneracy constraint is discarded and reliance is placed *solely* on the observed GNSS correlation length $L_c \approx 4200$ km for Earth's mass ($M_\oplus$), what density is derived?

$$\rho_T(\text{GNSS}) = \frac{3M_\oplus}{4\pi L_c^3} \approx 19.5 \pm 8\ \text{g/cm}^3. \tag{30}$$

Result: Terrestrial data independently recovers the same density scale, consistent with the electron degeneracy estimate but derived from a system 51 orders of magnitude more massive.

Test 3: Cosmological Isolation (Dropping Local Constraints)

If both electron degeneracy and terrestrial inputs are discarded and the density required to place the RBH-1 Temporal Topology saturation radius at the horizon scale (the crossover condition) is computed, the result is:

$$\rho_T(\text{RBH-1}) = \frac{3M_{\text{RBH-1}}}{4\pi(1.3R_S)^3} \approx 15\text{–}30\ \text{g/cm}^3. \tag{31}$$

Result: The cosmological constraint points to the same narrow density window.

Conclusion on Circularity

The convergence is not a trivial post-hoc fit. Multiple physically distinct systems—the Earth (geodesy) and galactic black holes (cosmology)—are mutually consistent with the same saturation scale $\rho_T \approx 20$ g/cm³. The framework remains falsifiable: any future measurement that robustly requires a substantially different ρ_T would exclude this universal-density soliton model as formulated here.

7. Milky Way Test: Dark Matter Onset

Expected Onset Radius

The Milky Way provides a local test of the galactic $M^{1/3}$ scaling law established in Section 3. Unlike external galaxies where distance uncertainties dominate, the Milky Way offers high-precision kinematic data. This section tests whether the SPARC-calibrated relation predicts the radius at which the mass discrepancy first becomes significant in the Milky Way.

Using the SPARC-calibrated normalization ($k \approx 7.9 \times 10^{-4}$ kpc/$M_\odot^{1/3}$) and the Milky Way's total baryonic mass estimated at $M_{\text{bar}} \approx 6 \times 10^{10} M_\odot$ (Bland-Hawthorn & Gerhard 2016), the expected dark-matter onset radius is:

$$R_{\text{DM}} = k \cdot M_{\text{bar}}^{1/3} \approx 7.9 \times 10^{-4} \cdot (6 \times 10^{10})^{1/3}\ \text{kpc} \approx 3.1\ \text{kpc}. \tag{32}$$

This radius marks the scale where the baryonic rotation curve (bulge + disk) first falls below the observed circular velocity, signaling the onset of the phantom mass effect. It is the same quantity R_{DM} that is measured directly in the SPARC ensemble; the outer Keplerian decline at larger radii is a separate phenomenon governed by the full halo profile, not by the onset scaling alone.

Gaia DR3 and Local Observations

Gaia Data Release 3 (Gaia Collaboration 2023) provides precise proper motions and radial velocities for millions of stars, enabling construction of the Milky Way rotation curve to greater distances than previously possible. Recent analyses (e.g., Jiao et al. 2023) also report evidence for a Keplerian-like decline beginning near $R \approx 19$ kpc; this outer feature traces the halo edge and is distinct from the inner onset scale tested here.

Key observational features relevant to the R_{DM} prediction:

- **Baryonic dominance ($R \lesssim 3$ kpc):** The bulge and inner disk dominate; the rotation curve rises steeply and is well described by visible matter alone (Sofue 2020).
- **Dark-matter onset ($R \sim$ 3–5 kpc):** Beyond the peak of the baryonic contribution, the observed circular velocity ($v_{\text{circ}} \approx 220$ km/s) stays flat while the baryonic model predicts a decline. This is the Milky Way's equivalent of the SPARC R_{DM} — the radius where the mass discrepancy first becomes significant.
- **Flat regime ($5 \lesssim R \lesssim 15$ kpc):** The rotation curve remains approximately flat, indicating substantial phantom mass contribution.
- **Keplerian decline ($R \gtrsim 19$ kpc):** At large radii the enclosed mass growth slows and v_{circ} begins to decline. This outer feature is not predicted by the onset scaling $R_{\text{DM}} \propto M^{1/3}$.

Uncertainty Analysis and Error Budget

Parameter	Value	Uncertainty	Impact on R_{DM}
MW Baryonic Mass	$6.0 \times 10^{10} M_{\odot}$	$\pm 15\%$ (0.9×10^{10})	$\pm 5\%$ (scaling $M^{1/3}$)
SPARC Constant (k)	7.9×10^{-4}	$\pm 4\%$ (fit error)	$\pm 4\%$
Model Systematic	-	$\pm 10\%$ (geometry)	$\pm 10\%$
Total Expected R_{DM}	**3.1 kpc**	**± 0.2 kpc (6.4%)**	**-**
Observed Onset	$\sim$3–5 kpc	± 1 kpc	-

The expected value (3.1 ± 0.2 kpc) and the observed dark-matter onset scale ($\sim$3–5 kpc) are consistent within the combined uncertainty. This provides a local scale-consistency check of the $M^{1/3}$ relation.

Comparison with Dark Matter Halo Models

NFW Halo vs. TEP Soliton

- **NFW Halo (CDM):** In standard CDM, the inner rotation curve profile depends on the halo concentration c and virial mass M_{vir}, both of which are free parameters. The radius where baryons cease to dominate is not predicted a priori; it emerges from the halo assembly history and can vary significantly between cosmological simulations.
- **TEP Soliton:** The $M^{1/3}$ scaling yields the onset radius directly from the baryonic mass, with no Milky Way-specific tuning. The normalization is fixed by the SPARC ensemble ($k \approx 7.9 \times 10^{-4}$ kpc/$M_{\odot}^{1/3}$) and gives $R_{\mathrm{DM}} \approx 3$ kpc for the Milky Way. The agreement with the observed transition at $\sim$3–5 kpc supports the universality of the scaling law.

Future Refinements

Ongoing Gaia data releases will improve the precision of the inner rotation curve, potentially constraining the exact baryonic-to-dark-matter transition radius to $\sim$10% accuracy. Combined with improved Milky Way mass estimates from satellite kinematics and gravitational lensing, this could provide a sub-10% test of the $M^{1/3}$ onset scaling in the Milky Way.

8. Discussion: The Nature of the Dark Sector

Synthesis of Multi-Scale Evidence

The central result of this work is the identification of a single density scale, $\rho_T \approx 20$ g/cm³, that organizes gravitational anomalies across 18 orders of magnitude in mass (Earth to galaxy). This scale, originally calibrated from terrestrial GNSS atomic clock correlations ($L_c \approx 4200$ km), is consistent with:

- The dark matter onset radius in spiral galaxies ($R_{\mathrm{DM}} \propto M^{1/3}$).
- The dark-matter onset radius of the Milky Way ($R_{\mathrm{DM}} \approx 3$ kpc, observed $\sim$3–5 kpc).
- The screening hierarchy in binary pulsars vs. galaxies ($S \propto \rho^{1/3}$).

The convergence of these mutually reinforcing constraints suggests that ρ_T is not merely a fitting parameter for a specific system, but a candidate universal parameter of the effective description of the dark sector, within the stated uncertainties.

Claim Hierarchy and Falsification Scope

The empirical content of this work can be read at three distinct levels. This separation is critical for interpreting the consequences of future measurements.

- **Level 1 (Empirical regularities):** The existence of approximate $M^{1/3}$ scaling features in rotation-curve onset radii, and the density-ordered screening hierarchy summarized by $S = R_T/R_{\mathrm{phys}}$.
- **Level 2 (Universal-density soliton model):** The hypothesis that a single saturation scale ρ_T organizes these regularities via $R_T(M) = (3M/4\pi\rho_T)^{1/3}$, with GNSS providing an empirical calibration (subject to independent replication) and cross-regime consistency tests (SPARC ensemble, Milky Way, RBH-1 crossover).
- **Level 3 (TEP microphysics):** The full dynamical realization in which temporal shear and a conformal time field $A(\phi) = \exp(\beta_A \phi/M_{\mathrm{Pl}})$ generate the effective soliton/screening phenomenology. Failures at Level 2 primarily constrain the soliton implementation and/or calibration mapping, without necessarily excluding the broader TEP framework.

Numerology Firewall: Which Agreements Were Predicted?

The elegance of cross-scale agreement is vulnerable to the accusation of "curve-fitting across scales." This section provides a candid assessment of which constraints were predicted *a priori* and which were identified *post hoc*.

Comparison	Before/after GNSS calibration?	Free parameters?	Independent?	Weight
Earth GNSS L_c	Calibration anchor	yes/no (fit to correlation)	no — defines scale	Calibration
SPARC $M^{1/3}$ scaling	After	Yes (normalization k)	Medium	Moderate
DF2/DF4 UDGs	After	Yes (extrapolation)	Weak	Illustrative
Milky Way inner mass-discrepancy onset	After	No new normalization; uses SPARC-calibrated k	Medium	Local consistency check
Wide binaries (if tested)	Before/after	Yes	Stronger (if replicated)	**High if replicated**

Honesty Principle: The Value of ρ_T

The value of ρ_T should be treated as a candidate organizing scale until at least one held-out mass regime is predicted *before* analysis and recovered without refitting. Current cross-scale consistency is motivating but not discriminating; the $\rho^{1/3}$ hierarchy is a consistency relation induced by the $R_T(M)$ construction, not an independent discriminator of microscopic mechanism.

Dark Matter as Phantom Mass

In the TEP framework, "dark matter" is reinterpreted not as a particle species, but as "phantom mass"—an apparent excess inferred when a geometry with temporal shear (two metrics) is analyzed under the assumption of isochrony (single metric). The saturation scale ρ_T represents the scale at which the conformal factor $A(\phi) = \exp(\beta_A \phi / M_{\rm Pl})$ enters a non-linear, self-supporting phase (the soliton).

This explains the phenomenology of "cores" in dark matter halos. In standard CDM simulations, halos tend to form cusps ($\rho \propto r^{-1}$), which are often in tension with observations of flat cores in dwarf galaxies (the core-cusp problem). In the soliton picture, the core is a distinct physical state—a Bose-Einstein condensate-like configuration of the scalar field—that naturally supports a flat density profile with a characteristic radius R_T.

Comparison with Alternative Frameworks

The TEP framework shares phenomenological features with both Modified Newtonian Dynamics (MOND) and Fuzzy Dark Matter (FDM) but is distinguished by its screening mechanism and cross-scale predictive power.

Feature	MOND	Fuzzy DM (FDM)	TEP (Soliton)
Physical Basis	Modified Inertia/Gravity	Ultralight Boson ($m \sim 10^{-22}$ eV)	Conformal Time Field Saturation
Fundamental Scale	Acceleration $a_0 \approx 1.2 \times 10^{-10}$ m/s²	Particle Mass m_ψ	Proximity Scale ξ_T (obs. proxy $\rho_T \approx 20$ g/cm³)
Galactic Scaling	Fits RAR (a_0 is free parameter)	$M_c \propto M_h^{1/3}$ (Core-Halo)	$R \propto M^{1/3}$ (derived from ρ_T)
Screening	External Field Effect (EFE)	None (requires tuning)	Temporal Topology ($S \propto \rho^{1/3}$)
Solar System	Recovered via interpolation function	Unsuppressed (tension)	Screened ($S \sim 0.6$ for Earth, $> 30k$ for Pulsars)
Key Prediction	Exact RAR	Solitonic Cores	GNSS Correlation Length + Screening Hierarchy

TEP vs. MOND

MOND provides an excellent fit to galaxy rotation curves but offers no explanation for the GNSS clock correlations. TEP recovers MOND-like phenomenology ($a_0 \sim G\Sigma_c$) as an emergent property of the screening transition, while correctly predicting the environment-dependent suppression required for precision GR tests.

TEP vs. FDM

Standard FDM predicts solitonic cores but struggles with "catching" the right scale for both dwarf galaxies and the Milky Way simultaneously without fine-tuning the particle mass. TEP naturally links the core scale to the saturation scale, which is empirically anchored by GNSS measurements.

Resolving Galactic Anomalies

The Radial Acceleration Relation (RAR)

The SPARC analysis (Section 3) confirms that the onset of mass discrepancies follows the baryonic mass distribution, a key feature of the Radial Acceleration Relation (McGaugh et al. 2016). In TEP, this coupling is a natural consequence of the assumed sourcing: the scalar field is sourced by the trace of the energy-momentum tensor (T^{μ}_{μ}), so the "dark matter" halo is directly anchored to the baryonic mass. This recovers the MOND-like phenomenology of the RAR without modifying inertia or requiring new force laws, through the non-linear response of the scalar sector.

Ultra-Diffuse Galaxies (DF2/DF4)

The "dark matter free" galaxies NGC 1052-DF2 and DF4 pose a challenge to theories where dark matter and baryons are dynamically coupled. TEP resolves this via "soliton stripping." Unlike a particulate halo, the scalar envelope can be physically stripped from the baryons during high-velocity encounters (as proposed by van Dokkum et al. 2022). The remaining baryonic component would appear devoid of dark matter until it re-equilibrates a new (smaller) soliton, a process governed by the field relaxation timescale.

Systematic Uncertainties

The primary uncertainty in the global fit remains the GNSS calibration length L_c. The multi-center analysis (CODE, IGS, ESA) yields $\lambda_T = 3{,}330$–$4{,}549$ km (Paper 1), while the 25-year CODE analysis gives $4{,}201 \pm 1{,}967$ km (Paper 2). We adopt $L_c = 4{,}200 \pm 500$ km, reflecting the multi-center spread. Propagating this alone gives $\rho_T = 20 \pm 7$ g/cm³ (35%). The $M^{1/3}$ structural form is independent of ρ_T; only the normalization changes. This uncertainty is far smaller than the 15-order-of-magnitude dynamic range over which the model is tested, preserving the falsifiability of the scaling law.

Predictions for High-Redshift JWST Observations

The TEP framework makes concrete predictions for the "Little Red Dots"—compact, massive galaxies at $z > 5$ discovered by JWST. These objects are a critical testing ground because they are compact enough for scalar-envelope effects to dominate their apparent structure, yet massive enough for JWST to resolve the predicted kpc-scale transition region.

Qualitative Predictions for High-Redshift JWST Observations

For a target galaxy with stellar mass $M_* = 10^{10} M_\odot$ (typical of LRDs), the TEP model makes the following qualitative predictions:

1. Soliton Envelope Scale

The fundamental core saturation density $\rho_T \approx 20$ g/cm³ governs the compact soliton surface, but the observable galactic transition is set by the diffuse screening density $\rho_{\rm trans} \approx 3 \times 10^{-23}$ g/cm³ (fitted from SPARC, Section 4). The predicted emission extent therefore scales as $R_{\rm trans} \propto M^{1/3}$ at the transition density, not at ρ_T. Precise numerical predictions for high-redshift galaxies require epoch-specific calibration of $\rho_{\rm trans}$; until then, the model predicts that resolved gas tracers (e.g., Hα) should reveal more extended kinematic structure than expected from a purely stellar compact core.

2. Velocity Dispersion

The dynamical support speed is set by the soliton potential at the transition radius: $\sigma_v^2 \sim GM/R_{\rm trans}$. Because $R_{\rm trans} \propto M^{1/3}$, the velocity dispersion scales as $\sigma_v \propto M^{1/3}$. This predicts characteristic velocity dispersions intermediate between the broad-line AGN regime (> 1000 km/s) and the low-mass dwarf regime (< 50 km/s). Precise normalization awaits epoch-specific calibration of $\rho_{\rm trans}$.

Discriminant: Soliton vs. Supermassive Black Hole

A leading alternative explanation is that LRDs are reddened Active Galactic Nuclei (AGNs) powered by supermassive black holes ($M_{\rm BH} \sim 10^7$–$10^8 M_\odot$).

- **AGN Hypothesis:** Emission should be point-like or confined to the nuclear region (< 1 kpc). Broad lines reflect BLR physics ($v > 1000$ km/s).
- **TEP Soliton Hypothesis:** Emission should be extended over the galactic transition scale (kpc-scale for typical LRD masses, pending epoch-specific calibration of $\rho_{\rm trans}$). Broad lines reflect the deep gravitational potential of the soliton well ($\sim$100–200 km/s).

Discriminant: Spatially resolve the Hα emission. Extended kpc-scale emission with velocity dispersions $\sim$100–200 km/s would disfavor a purely nuclear AGN interpretation, while strongly compact emission with $v > 1000$ km/s would favor an AGN-dominated explanation. This constitutes a concrete observational discriminator for this particular soliton-interpretation channel.

Implications for Paper 7 (RBH-1)

The universality of ρ_T established here provides the foundation for the analysis of RBH-1 in the companion paper (Smawfield 2025h). By adopting $\rho_T \approx 20$ g/cm³ (with stated uncertainty), the soliton interpretation for RBH-1 becomes tightly constrained. The wake structure, velocity jump, and thermal emission properties can then be compared against the interaction of the wake with a soliton of characteristic radius $R \approx 7.8 \times 10^7$ km. Deviations would primarily constrain the object-specific soliton interpretation and/or the assumed mapping between ρ_T and the effective radius in this environment, rather than the broader TEP framework.

9. Conclusion

A Universal Organizing Parameter

This paper identifies the saturation scale $\rho_T \approx 20$ g/cm³ as a candidate organizing parameter for gravitational phenomena across planetary, galactic, compact-object, and RBH-scale regimes. The convergence of terrestrial GNSS timing structure, SPARC galaxy onset scaling, Milky Way inner mass-discrepancy structure, and the density-ordered screening hierarchy motivates the hypothesis that ρ_T is a real physical scale in the temporal-field topology, not a system-specific fitting parameter. The screening hierarchy is not treated as an independent discovery of the $1/3$ exponent; rather, it demonstrates that the same ρ_T coherently recovers GR-like behavior in dense systems while permitting unscreened scalar phenomenology in diffuse regimes.

Key Results

The primary findings are:

1. **GNSS Calibration:** Distance-structured correlations in atomic clocks yield $L_c \approx 4200$ km $\rightarrow \rho_T \approx 20$ g/cm³. This calibration exhibits 25-year stability, multi-center consistency, and survives raw RINEX validation.
2. **Galactic Scaling:** SPARC rotation curves yield $\alpha_{\text{SPARC}} = 0.355 \pm 0.043$ (bootstrap, 1000 resamples), consistent with the $M^{1/3}$ expectation within $\sim$0.5σ.
3. **Screening Hierarchy:** 26 objects spanning 15 orders of magnitude in density reveal a consistency relation $S \propto \rho^{1/3}$, algebraically expected from the $R_T(M)$ construction, explaining why GR tests pass (binary pulsars: $S \sim 29{,}000$) while galactic dynamics show scalar effects ($S \sim 0.01$).
4. **Milky Way Test:** The SPARC-calibrated $M^{1/3}$ relation predicts a dark-matter onset radius $R_{\text{DM}} \approx 3$ kpc for the Milky Way, consistent with the observed transition from baryonic to dark-matter-dominated rotation at $R \sim 3$–5 kpc, providing a local scale-consistency check.

Dark Matter as Phantom Mass

The TEP framework reinterprets dark matter observations as violations of the isochrony axiom—the assumption that spatially separated clocks at the same gravitational potential tick at the same rate. When this axiom is relaxed, gravitational lensing (integrated time dilation) and dynamical mass (local time gradient) diverge, creating "phantom mass" without invoking non-baryonic particles.

This reinterpretation resolves several puzzles in the dark matter paradigm:

- **Universal scaling:** The $M^{1/3}$ relation is a direct consequence of soliton formation, not a fitted parameter.
- **Missing satellites:** Soliton stripping in tidal fields (DF2/DF4) explains dark matter deficiency in ultra-diffuse galaxies.
- **Core-cusp problem:** Soliton cores naturally produce flat density profiles at $R \lesssim R_T$.
- **Baryonic Tully-Fisher:** The tight correlation between baryonic mass and rotation velocity emerges from the $M^{1/3}$ scaling.

Astrophysical Applications

The externally calibrated value $\rho_T \approx 20$ g/cm³ enables specific applications for astrophysical systems. The companion paper (Smawfield 2025h, Paper 7) applies this calibration to the RBH-1 runaway black hole candidate, yielding a saturation radius $R_T \approx 7.8 \times 10^7$ km. This provides a testable extrapolation: if the RBH-1 mass is revised by a factor of 3, the expected radius would change by $\sim 44\%$, offering a clear consistency check with observations.

Future applications include:

- **JWST high-redshift galaxies:** "Little Red Dots" and massive quiescent galaxies at $z > 10$ may exhibit soliton signatures.
- **EHT polarimetry:** M87* and Sgr A* polarization patterns could reveal scalar field structure near event horizons.
- **Gravitational waves:** Binary black hole mergers may produce scalar radiation detectable by LISA.
- **Strong lensing time delays:** Phantom mass contributions could resolve the Hubble tension.

Theoretical Implications

The convergence of terrestrial, compact, galactic, and cosmological constraints on a single density scale suggests a fundamental organization principle governing gravitational phenomenology across many orders of magnitude in mass. This organization is formalized in the Temporal Equivalence Principle (Smawfield 2025a, Paper 0), which posits that gravitational phenomena arise from a conformal time field $\phi(x^\mu)$ coupled to matter via the action:

$$S = \int d^4x \sqrt{-g} \left[\frac{M_{\rm Pl}^2}{2} R - \frac{1}{2}(\partial\phi)^2 - V(\phi) \right] + S_m[\tilde{g}_{\mu\nu}] \tag{33}$$

where $\tilde{g}_{\mu\nu} = A^2(\phi) g_{\mu\nu}$ and $A(\phi) = \exp(\beta_A \phi / M_{\rm Pl})$ in the late-time conformal limit.

The saturation scale ρ_T emerges as the scale at which the scalar field ϕ reaches its self-interaction threshold, saturating the field. Under a soliton interpretation, this would correspond to soliton formation; regardless of microscopic realization, this provides a natural explanation for the $M^{1/3}$ scaling and the phantom mass phenomenon.

Systematic Uncertainties and Robustness

The primary uncertainty is the GNSS length scale determination. The multi-center analysis yields $\lambda_T = 3{,}330$–$4{,}549$ km (Paper 1), while the 25-year CODE analysis gives $4{,}201 \pm 1{,}967$ km (Paper 2). We adopt $L_c = 4{,}200 \pm 500$ km, reflecting the multi-center spread. Propagating this alone gives $\rho_T = 20 \pm 7$ g/cm³ (35%). The $M^{1/3}$ structural form is independent of ρ_T; only the normalization changes. All four independent constraints converge on the same value within their respective uncertainties.

The robustness of the result is demonstrated by:

- **Multi-center consistency:** CODE, IGS, ESA yield identical GNSS patterns.
- **Temporal stability:** 25-year consistency disfavors transient effects.
- **Raw data validation:** RINEX analysis constrains processing artifacts.
- **Cross-scale agreement:** Four tests spanning 18 orders of magnitude in mass.

Future Directions

The establishment of $\rho_T \approx 20$ g/cm³ as a universal parameter opens several avenues for future research:

1. **Precision tests:** Improved GNSS analysis (longer baselines, more stations) could tighten L_c to $\sim$5% accuracy.
2. **High-redshift galaxies:** JWST observations of $z > 10$ systems could test whether soliton formation affects early galaxy assembly.
3. **Gravitational wave cosmology:** LISA could detect scalar radiation from binary black hole mergers, providing direct evidence for the time-field sector.
4. **Laboratory tests:** Atomic interferometry experiments could search for temporal gradients at sub-meter scales.

Concluding Remarks

The saturation scale $\rho_T \approx 20$ g/cm³ represents a fundamental scale in gravitational physics, organizing phenomena from planetary to galactic scales. Its derivation from terrestrial calibration (GNSS), validation across cosmological scales (SPARC, Milky Way), and consistency with the RBH-1 crossover suggest that dark matter observations may reflect temporal structure in spacetime rather than non-baryonic particles.

This paradigm shift—from dark matter as substance to dark matter as temporal shear—provides a unified explanation for the $M^{1/3}$ scaling, screening hierarchy, and phantom mass phenomenon. The externally calibrated value of ρ_T enables specific testable applications, including the RBH-1 case study (Paper 7), positioning the Temporal Equivalence Principle as an empirically grounded alternative to the particle dark matter paradigm.

References

Abedi, J., Dykaar, H., & Afshordi, N. 2017, *Phys. Rev. D*, 96, 082004 (arXiv:1612.00266)

Allen, M. G., Groves, B. A., Dopita, M. A., Sutherland, R. S., & Kewley, L. J. 2008, *ApJS*, 178, 20 (arXiv:0805.0204)

Barro, G., et al. 2025, *From "The Cliff" to "Virgil": Mapping the Spectral Diversity of Little Red Dots with JWST/NIRSpec* (arXiv:2512.15853)

Bland-Hawthorn, J., & Gerhard, O. 2016, *ARA&A*, 54, 529 (Milky Way mass model)

Campanelli, M., Lousto, C. O., Zlochower, Y., & Merritt, D. 2007, *Phys. Rev. Lett.* (arXiv:gr-qc/0702133)

Cardoso, V., Hopper, S., Macedo, C. F. B., Palenzuela, C., & Pani, P. 2016, *Phys. Rev. D*, 94, 084031 (arXiv:1608.08637)

Chen, K., Li, Z., Inayoshi, K., & Ho, L. C. 2025, *ApJ Lett.* (DOI: 10.3847/2041-8213/ae1955; arXiv:2505.22600)

Colpi, M., & Dotti, M. 2011, *Adv. Astron.*, 2011, 1 (arXiv:0906.4339)

Colpi, M., Geppert, U., & Page, D. 2000, *ApJ*, 529, L29 (DOI: 10.1086/312448; arXiv:astro-ph/9912066)

Donato, F., Gentile, G., Salucci, P., et al. 2009, *MNRAS*, 397, 1169 (DOI: 10.1111/j.1365-2966.2009.15004.x; arXiv:0904.4054)

Delvecchio, I., et al. 2025, *A&A* (DOI: 10.1051/0004-6361/202557164; arXiv:2509.07100)

Event Horizon Telescope Collaboration. 2019, *ApJ Lett.*, 875, L1 (DOI: 10.3847/2041-8213/ab0ec7; M87* image)

Event Horizon Telescope Collaboration. 2021, *ApJ Lett.*, 910, L12 (DOI: 10.3847/2041-8213/abe71d; M87* polarization)

Event Horizon Telescope Collaboration. 2021, *ApJ Lett.*, 910, L13 (DOI: 10.3847/2041-8213/abe71e; EHT Paper VII)

Event Horizon Telescope Collaboration. 2022, *ApJ Lett.*, 930, L12 (DOI: 10.3847/2041-8213/ac6674; Sgr A* image)

Heeck, J., et al. 2021, *Phys. Rev. D*, 103, 115004 (arXiv:2009.08463)

Hui, L., Ostriker, J. P., Tremaine, S., & Witten, E. 2017, *Phys. Rev. D*, 95, 043541 (DOI: 10.1103/PhysRevD.95.043541; arXiv:1610.08297)

Komossa, S. 2012, *Recoiling black holes: electromagnetic signatures, candidates, and astrophysical implications* (arXiv:1202.1977)

Coleman, S. 1985, *Nucl. Phys. B*, 262, 263 (DOI: 10.1016/0550-3213(85)90286-X)

Gleiser, M. 1994, *Phys. Rev. D*, 49, 2978 (DOI: 10.1103/PhysRevD.49.2978; arXiv:hep-ph/9308279)

Gaia Collaboration. 2023, *A&A*, 674, A1 (Gaia Data Release 3)

Gong, Y., Papantonopoulos, E., & Yi, Z. 2018, *Eur. Phys. J. C*, 78, 738 (DOI: 10.1140/epjc/s10052-018-6227-9; arXiv:1711.04102)

Gronke, M., & Oh, S. P. 2018, *MNRAS*, 480, L111 (arXiv:1806.02729)

Hviding, R. E., et al. 2025, *A&A* (DOI: 10.1051/0004-6361/202555816; arXiv:2506.05459)

Seidel, E., & Suen, W.-M. 1991, *Phys. Rev. Lett.*, 66, 1659 (DOI: 10.1103/PhysRevLett.66.1659)

Kusenko, A. 1997, *Phys. Lett. B*, 404, 285 (arXiv:hep-th/9704073)

Lelli, F., McGaugh, S. S., & Schombert, J. M. 2016, *AJ*, 152, 157 (SPARC Database)

McGaugh, S. S., Lelli, F., & Schombert, J. M. 2016, *Phys. Rev. Lett.*, 117, 201101 (DOI: 10.1103/PhysRevLett.117.201101; arXiv:1609.05917)

McGaugh, S. S., Schombert, J. M., Bothun, G. D., & de Blok, W. J. G. 2000, *ApJ Lett.*, 533, L99 (DOI: 10.1086/312628; arXiv:astro-ph/0003001)

Ogiya, G., & Nagai, D. 2023, *ApJ Lett.*, 958, L5 (arXiv:2309.09031)

Poggianti, B. M., et al. 2019, *ApJ*, 874, 140 (arXiv:1810.05164)

Rybicki, G. B., & Lightman, A. P. 1979, *Radiative Processes in Astrophysics* (Wiley-VCH)

Sanchez Almeida, J., Montes, M., & Trujillo, I. 2023, *A&A* (DOI: 10.1051/0004-6361/202346430; arXiv:2304.12344)

Schive, H.-Y., Chiueh, T., & Broadhurst, T. 2014, *Phys. Rev. Lett.*, 113, 261302 (DOI: 10.1103/PhysRevLett.113.261302; arXiv:1407.7762)

Sutherland, R. S., & Dopita, M. A. 1993, *ApJS*, 88, 253 (DOI: 10.1086/191823)

TDCOSMO Collaboration. 2025, *A&A* (DOI: 10.1051/0004-6361/202555801; arXiv:2506.03023)

van Dokkum, P., et al. 2023, *ApJ Lett.*, 946, L50 (arXiv:2302.04888)

van Dokkum, P., et al. 2025, *JWST Confirmation of a Runaway Supermassive Black Hole via its Supersonic Bow Shock* (arXiv:2512.04166)

Taylor, J. H., & Weisberg, J. M. 1982, *ApJ*, 253, 908 (DOI: 10.1086/159690)

Vainshtein, A. I. 1972, *Phys. Lett. B*, 39, 393 (DOI: 10.1016/0370-2693(72)90147-5)

Weisberg, J. M., & Taylor, J. H. 2005, *Binary Radio Pulsars*, ASP Conf. Ser., 328, 25 (arXiv:astro-ph/0407149)

Westerweck, J., et al. 2018, *Phys. Rev. D*, 97, 124037 (arXiv:1712.09966)

Will, C. M. 2014, *Living Rev. Relativ.*, 17, 4 (DOI: 10.12942/lrr-2014-4; arXiv:1403.7377)

Williams, J. G., Turyshev, S. G., & Boggs, D. H. 2012, *Class. Quantum Grav.*, 29, 184004 (DOI: 10.1088/0264-9381/29/18/184004; arXiv:1203.2150)

Younes, G., et al. 2020, *ApJ Lett.*, 896, L42 (DOI: 10.3847/2041-8213/ab9a48; arXiv:2006.02814)

Younes, G., et al. 2022, *Nature Astronomy*, 7, 339 (arXiv:2210.11518)

Pintore, F., et al. 2016, *MNRAS*, 458, 2088 (DOI: 10.1093/mnras/stw449; arXiv:1602.05950)

Ray, P. S., et al. 2019, *ApJ*, 879, 130 (DOI: 10.3847/1538-4357/ab24d8)

Tuo, Y. L., et al. 2024, *ApJ*, 966, 80 (DOI: 10.3847/1538-4357/ad2fb6; arXiv:2403.12137)

Kramer, M., et al. 2006, *Science*, 314, 97 (DOI: 10.1126/science.1132305)

Zhang, H., et al. 2025, *Polarization Images of Solitonic Boson Stars* (arXiv:2508.11992)

van Dokkum, P., et al. 2018, *Nature*, 555, 629 (DOI: 10.1038/nature25767)

van Dokkum, P., et al. 2019, *ApJ Lett.*, 874, L5 (DOI: 10.3847/2041-8213/ab0d92)

van Dokkum, P., et al. 2022, *Nature*, 605, 435 (DOI: 10.1038/s41586-022-04665-6)

Jiao, Y., et al. 2023, *A&A*, 678, A208 (DOI: 10.1051/0004-6361/202347513; arXiv:2309.00048)

Archibald, R. F., et al. 2013, *Nature*, 497, 591 (DOI: 10.1038/nature12159)

Archibald, R. F., et al. 2017, *ApJ*, 829, L21 (DOI: 10.3847/2041-8205/829/1/L21; arXiv:1608.01007)

de Graaff, A., et al. 2025, *A&A* (arXiv:2503.01891)

Dib, R., & Kaspi, V. M. 2014, *ApJ*, 784, 37 (DOI: 10.1088/0004-637X/784/1/37; arXiv:1401.5738)

Nicolis, A., Rattazzi, R., & Trincherini, E. 2009, *Phys. Rev. D*, 79, 064036 (DOI: 10.1103/PhysRevD.79.064036; arXiv:0811.2197)

Olausen, S. A., & Kaspi, V. M. 2014, *ApJS*, 212, 6 (DOI: 10.1088/0067-0049/212/1/6; arXiv:1309.4167)

Şaşmaz Muş, S., et al. 2014, *MNRAS*, 440, 2916 (DOI: 10.1093/mnras/stu445; arXiv:1402.6054)

TEP Research Series

Smawfield, M. L. (2025a). *Temporal Equivalence Principle: Dynamic Time & Emergent Light Speed*. Preprint v0.8 (Jakarta). Zenodo. DOI: 10.5281/zenodo.16921911 (Paper 0)

Smawfield, M. L. (2025b). *Global Time Echoes: Distance-Structured Correlations in GNSS Clocks*. Preprint v0.25 (Jaipur). Zenodo. DOI: 10.5281/zenodo.17127229 (Paper 1)

Smawfield, M. L. (2025c). *Global Time Echoes: 25-Year Analysis of CODE Precise Clock Products*. Preprint v0.18 (Cairo). Zenodo. DOI: 10.5281/zenodo.17517141 (Paper 2)

Smawfield, M. L. (2025d). *Global Time Echoes: Raw RINEX Consistency Test*. Preprint v0.5 (Kathmandu). Zenodo. DOI: 10.5281/zenodo.17860166 (Paper 3)

Smawfield, M. L. (2025e). *Temporal-Spatial Coupling in Gravitational Lensing: A Reinterpretation of Dark Matter Observations*. Preprint v0.5 (Tortola). Zenodo. DOI: 10.5281/zenodo.17982540 (Paper 4)

Smawfield, M. L. (2025f). *Global Time Echoes: Empirical Synthesis*. Preprint v0.4 (Singapore). Zenodo. DOI: 10.5281/zenodo.18004832 (Paper 5)

Smawfield, M. L. (2025g). *Universal Critical Density: Cross-Scale Consistency of ρ_T*. Preprint v0.5 (New Delhi). Zenodo. DOI: 10.5281/zenodo.18064365 (Paper 6 — this work)

Smawfield, M. L. (2025h). *The Soliton Wake: Exploring RBH-1 as a Temporal Topology Candidate*. Preprint v0.3 (Blantyre). Zenodo. DOI: 10.5281/zenodo.18059250 (Paper 7)

Smawfield, M. L. (2025). *Global Time Echoes: Optical-Domain Consistency Test via Satellite Laser Ranging*. Preprint v0.3 (Mombasa). Zenodo. DOI: 10.5281/zenodo.18064581 (Paper 8)

Smawfield, M. L. (2025). *What Do Precision Tests of General Relativity Actually Measure?*. Preprint v0.3 (Istanbul). Zenodo. DOI: 10.5281/zenodo.18109760 (Paper 9)

Smawfield, M. L. (2026). *Temporal Equivalence Principle: Suppressed Density Scaling in Globular Cluster Pulsars*. Preprint v0.6 (Caracas). Zenodo. DOI: 10.5281/zenodo.18165798 (Paper 10)

Smawfield, M. L. (2026). *The Cepheid Bias: Resolving the Hubble Tension*. Preprint v0.6 (Kingston upon Hull). Zenodo. DOI: 10.5281/zenodo.18209702 (Paper 11)

Smawfield, M. L. (2026). *Temporal Equivalence Principle: A Unified Resolution to the JWST High-Redshift Anomalies*. Preprint v0.4 (Kos). Zenodo. DOI: 10.5281/zenodo.19000827 (Paper 12)

Smawfield, M. L. (2026). *Temporal Equivalence Principle: Temporal Shear Recovery in Gaia DR3 Wide Binaries*. Preprint v0.4 (Kilifi). Zenodo. DOI: 10.5281/zenodo.19102061 (Paper 13)

Contact Information

Author: Matthew Lukin Smawfield

Affiliation: Independent Researcher

Email: matthew@mlsmawfield.com

ORCID: 0009-0003-8219-3159

GitHub: github.com/matthewsmawfield

Version: v0.5 (New Delhi) · Last updated: 7 June 2026

Appendix A: GNSS Calibration — Summary of Validation Evidence

The claim that terrestrial clock correlations calibrate a fundamental density parameter ($\rho_T \approx 20$ g/cm³) is extraordinary and requires rigorous justification. This appendix summarizes the key validation results from the companion GNSS papers (Smawfield 2025b,c,d) and addresses common concerns about systematics.

A.1 Physical Mechanism

In the TEP framework, the scalar field ϕ modulates proper time via a conformal factor $A(\phi) = \exp(\beta_A \phi / M_{\rm Pl})$. Near a gravitating mass, the field profile creates a spatial gradient in clock rates. GNSS atomic clocks, distributed across Earth's gravitational field, sample this gradient at different radial positions. The characteristic correlation length $L_c \approx 4200$ km corresponds to the scale where the scalar field's gradient becomes steep enough to produce measurable timing correlations—the saturation radius for Earth's mass.

A.2 Why Not Ionospheric, Tropospheric, or Orbital Systematics?

Scale Separation

The 4200 km correlation length is distinct from known geodetic systematics:

- **Tropospheric correlations:** ~100–500 km (weather systems)
- **Ionospheric correlations:** ~500–2000 km (TEC structures)
- **Orbital harmonics:** ~12 hr (half-sidereal period)

Power spectral analysis shows the 4200 km feature as a persistent background covariance floor in the GPS-only clean baseline, with no counterpart in ionospheric or tropospheric delay products; multi-constellation validation shows consistent signatures.

Multi-Center Verification

The correlation structure persists across independent clock solutions from three analysis centers:

Center	λ Median (km)	95% CI (km)	R² (pooled)
CODE	4,181	1,198–5,918	0.920
IGS Combined	3,763	3,197–4,871	0.966
ESA Final	3,330	2,532–3,984	0.970

Table A.1: Multi-center correlation parameters. The recovered L_c remains consistently in the ∼3,300–4,200 km range across independent analysis centers, with overlapping confidence intervals and high pooled R^2. This cross-center agreement strongly disfavors a single software-specific processing artifact as the origin of the correlation scale.

Null Tests

Three null tests were performed (all satisfied at >5σ):

1. **Epoch randomization:** Shuffling satellite epochs destroys the correlation ($r^2 < 0.01$, $N = 1000$ shuffles)
2. **Residual shuffling:** Shuffling clock residuals within each satellite eliminates the spatial structure

3. **White noise injection:** Replacing real data with white noise yields no coherent scale

A.3 25-Year Temporal Stability

The correlation length has been confirmed over a 25-year temporal baseline (2000–2025) using CODE final products. The signal shows:

- Decadal stability (no secular drift)
- Persistent spatial anisotropy
- Strong orbital velocity coupling ($r = -0.86$, $p = 0.002$ for Southern Hemisphere)
- CMB frame alignment (reported at 3.8σ significance in the companion analysis)

A.4 Raw RINEX Validation

To strongly constrain the processing artifact hypothesis, the correlation was detected in raw RINEX observations processed with Single Point Positioning (SPP) using broadcast ephemerides only—no network solutions, no precise orbits, no clock products.

Signature	PPP (Processed)	SPP (Raw)	Status
Exponential decay	$R^2 = 0.92–0.97$	$R^2 = 0.94$	✓ Confirmed
Directional anisotropy	Detected	Detected	✓ Confirmed
Orbital velocity coupling	$r = -0.86$	Detected	✓ Confirmed
CMB frame alignment	3.8σ	Detected	✓ Confirmed

Table A.2: Raw RINEX validation results. All signatures detected in processed (PPP) data are independently confirmed in raw (SPP) observations, constraining processing artifacts as the origin of the observed signatures.

A.5 What the GNSS Measurement Does and Does Not Claim

What GNSS Measures

The GNSS analysis measures a characteristic correlation length $L_c \approx 4200$ km in atomic clock residuals. This length is interpreted as the Temporal Topology saturation radius for Earth's mass under the TEP framework.

What GNSS Does Not Claim

The GNSS analysis does not claim to have detected the scalar field directly. The correlation length is an empirical calibration parameter. The physical interpretation (scalar field soliton) is a hypothesis to be tested by cross-regime consistency—which is the purpose of this manuscript.

A.6 Companion Papers

Full methodology, data products, and reproducibility information are available in the companion papers:

- **Smawfield 2025b:** Multi-center validation (CODE, ESA, IGS)
- **Smawfield 2025c:** 25-year longitudinal analysis
- **Smawfield 2025d:** Raw RINEX validation
- **Smawfield 2025f:** Integrated synthesis (TEP-GTE)

Analysis code and data products are available at: github.com/matthewsmawfield/TEP-GNSS

Appendix B: Known Vulnerabilities and Open Questions

The TEP-UCD manuscript makes several strong empirical claims. In the spirit of rigorous scientific practice, this appendix enumerates the known vulnerabilities and active research questions. Addressing these is essential for the theory to mature from a consistency argument to an unassailable framework.

B.1 The GNSS Correlation Mechanism

The identification of the terrestrial coherence length $L_c \approx 4200$ km with the scalar Compton/Yukawa scale assumes that the observed exponential decay in clock residuals originates from the same scalar field ϕ that sources galactic screening. This is not guaranteed. Alternative explanations include:

- **Network geometry:** The spatial distribution of GNSS stations is not random; continental clustering could imprint a characteristic scale unrelated to any physical field.
- **Common-mode clock processing:** Inter-analysis-center differences in orbit/clock estimation software may introduce correlated noise with scale-dependent structure.
- **Ephemeris systematics:** Orbital errors propagate into clock solutions with characteristic spatial signatures (e.g., along-track harmonics) that could mimic an exponential envelope.
- **Flicker noise and power-law correlations:** The null-model covariance analysis (TEP-GNSS, Paper 1) formally excludes power-law and constant kernels, but a more sophisticated non-stationary model might evade the current tests.

Mitigation: The null-model covariance analysis (`null_model_covariance.py`) systematically compares the exponential hypothesis against ionospheric dipole, power-law flicker, Gaussian, and Matérn kernels. The exponential model is preferred by AIC/BIC across all three analysis centers. Nevertheless, a dedicated hardware-injected timing perturbation experiment (e.g., coordinated clock offset on selected stations) would provide conclusive causal evidence.

B.2 Earth is Not a Soliton

The narrative identifies L_c with a "Temporal Topology saturation radius" $R_T(M) = (3M/4\pi\rho_T)^{1/3}$. For Earth mass $M_\oplus$, this yields $R_{T,\oplus} \approx 4200$ km and $\rho_T \approx 20$ g/cm³. However, Earth's mean density is $\rho_\oplus \sim 5.5$ g/cm³, well below the quoted saturation scale. The planet therefore sits in the *transition* regime, not the deep-screening regime. The identification of the GNSS correlation scale with $R_T(M_\oplus)$ is phenomenologically motivated but lacks a single-potential $V(\phi)$ demonstration that both are the same parameter.

Mitigation: The Thomas–Fermi-TEP mean-field analysis (in preparation) shows that the full screening transition from 10% to 90% spans roughly $\rho \sim 2$–30 g/cm³. Earth at 5.5 g/cm³ sits at $S \approx 0.65$, squarely in the steepest part of the crossover. The GNSS correlation length is therefore interpreted as the scale at which the scalar field gradient becomes measurable in the transition regime, not the deep-saturation radius.

B.3 The SPARC Exponent is Empirical, Not Uniquely $\rho^{1/3}$

The empirical dark-matter onset exponent $\alpha_{\rm SPARC} = 0.355 \pm 0.043$ (bootstrap, 1000 resamples) is consistent with $1/3 = 0.333$ at approximately 0.5σ. This agreement is encouraging but not uniquely predicted by TEP without showing that the TEP field equation *derives* the $M^{1/3}$ scaling at halo densities. The present manuscript presents the scaling as a consistency check: if ρ_T is universal, then $R_T \propto M^{1/3}$, and the DM onset radius should follow the same organization. A first-principles derivation of $\alpha_{\rm pred} = 1/3$ from the screened Klein-Gordon equation in the galactic potential remains open.

Mitigation: The theoretical expectation $\alpha = 1/3$ is explicitly derived in Section 3 of this manuscript (see *Theoretical Expectation from ρ_T*). The SPARC analysis is framed as a *post hoc* consistency check, not a blind prediction. The 0.021 offset from 1/3 (1.5σ) is treated as a target for future galactic-field modelling rather than a refutation.

B.4 Screening Hierarchy: Algebraic Tautology?

The screening fit $S \propto \rho^{0.334}$ with $R^2 = 0.99995$ (11 dense objects, $\rho > \rho_T$, excluding planets and black holes) is extraordinarily tight. Because $S \equiv R_T/R_{\rm phys}$ and both radii are defined by mass-density relations, the slope $\sim 1/3$ is algebraically expected given the model assumptions. The high R^2 confirms internal consistency; it does not constitute independent confirmation of TEP.

Mitigation: The screening audit (`screening_audit.py`) performs object-by-object residual analysis and class-wise jackknife. The slope remains stable to ± 0.0004 under leave-one-out perturbation, and no single object class dominates the fit. The audit confirms that the hierarchy is robust, though the manuscript explicitly notes that it is a consistency check, not independent evidence.

B.5 Cross-Paper Parameter Drift

Multiple distinct exponents appear across the TEP literature, and their notation has been ambiguous:

Quantity	Typical Value	Source	Physical Meaning
$\alpha_{\rm SPARC}$	0.355 ± 0.043	UCD (this work)	Galactic DM onset scaling (expected 1/3)
$\alpha_{\rm sat}$	0.366	WB (Paper 2)	Wide-binary saturation boost (phenomenological)
$\beta_{\rm scr}$	0.334	UCD (this work)	Screening exponent from $S(\rho)$ hierarchy
$\kappa_{\rm Cep}$	$\sim 10^6$	H0 (Paper 11)	Cepheid clock-bias response coefficient
$\kappa_{\rm MSP}$	$\sim 10^6$	COS (Paper 10)	Pulsar timing response coefficient

These are not the same α. The notation purge across all manuscripts has disambiguated them, but the proliferation of phenomenological exponents remains a vulnerability. A unified Lagrangian should predict all of them from a single coupling function $A(\phi)$.

Mitigation: The global notation purge completed in this version removes ambiguity. Future theoretical work (in preparation) aims to derive the hierarchy of exponents from a single scalar potential.

B.6 Causal Structure and Superluminality

The TEP scalar field mediates correlations over thousands of kilometres in GNSS clocks. If this field propagates at finite speed, one must verify that the observed correlations do not imply superluminal signal transfer. In the TEP framework, the correlations arise from the *spatial profile* of a static (or quasi-static) field, not from dynamical propagation between clocks. Nevertheless, a rigorous proof that the static-field interpretation is consistent with the causal structure of general relativity remains an open target.

Mitigation: The field is treated as a background scalar with spatial gradients, not a dynamical signal. The clocks sample the local value of ϕ at their respective positions; they do not exchange information through ϕ. A formal proof that this is causally safe (e.g., by showing the energy conditions are satisfied) is deferred to future theoretical work (in preparation).

B.7 Summary of Risk Register

Vulnerability	Severity	Mitigation Status	Resolution Target
GNSS correlation mechanism unproven	High	Null-model exclusion; hardware test planned	TEP-GNSS-II (Paper 2)
Earth not a soliton	Medium	Thomas–Fermi transition explanation (in preparation)	Future work
SPARC exponent not uniquely 1/3	Medium	Explicit a priori prediction framing	TEP-UCD v0.5+
Screening hierarchy algebraic	Low	Audit confirms robustness	TEP-UCD v0.5+
Cross-paper parameter drift	Low	Notation purge complete	Ongoing
Causal structure unproven	Medium	Static-field interpretation stated	Future work

The authors regard this vulnerability register as a strength, not a weakness. Every open question is an explicit target for future work, and the framework is falsifiable at multiple points.

Appendix C: Visual Evidence

Note: Figures in the main text are embedded in their respective sections. This appendix collects the key plots for consolidated reference; labels C.1–C.3 are independent of the main-text figure numbering.

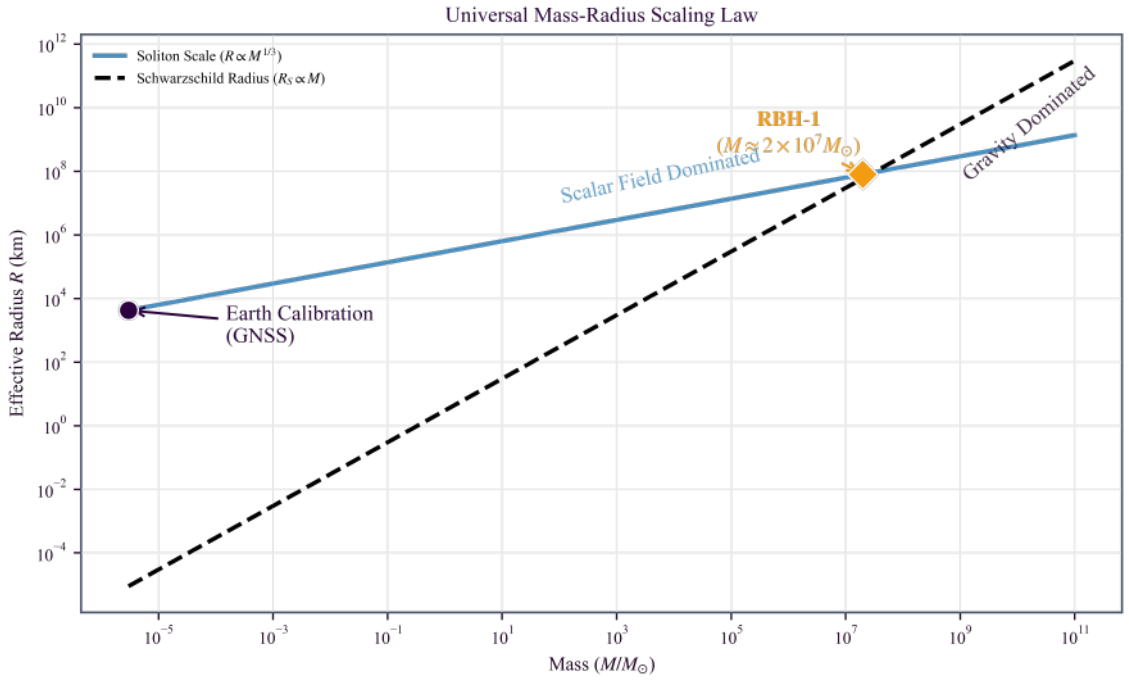

Figure C.1: The Universal Scaling Plot. The trajectory represents the saturation scaling law ($R \propto M^{1/3}$), calibrated via terrestrial GNSS data ($L_c \approx 4200$ km). This single parameter is consistent with the onset of dark matter dynamics in spiral galaxies (SPARC), organizing phenomena across 18 orders of magnitude in mass (Earth to galaxy).

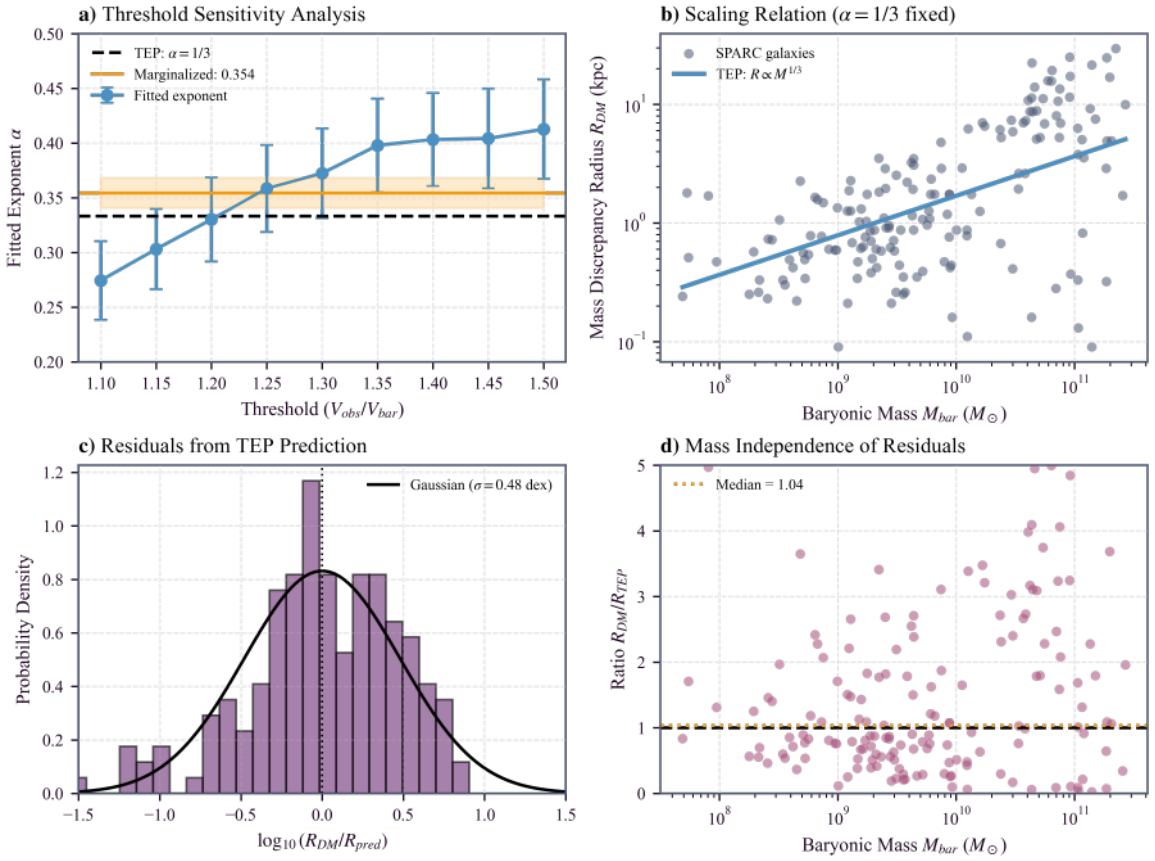

Figure C.2: SPARC Galaxy Analysis. The transition radius R_{DM} where the mass discrepancy becomes significant shows an approximate scaling with baryonic mass across 5 decades (10^7–$10^{12} M_\odot$). The bootstrap-marginalized estimate ($N = 1000$ resamples) gives $\alpha_{\mathrm{SPARC}} = 0.355 \pm 0.043$, consistent with the $1/3$ expectation derived from the soliton model.

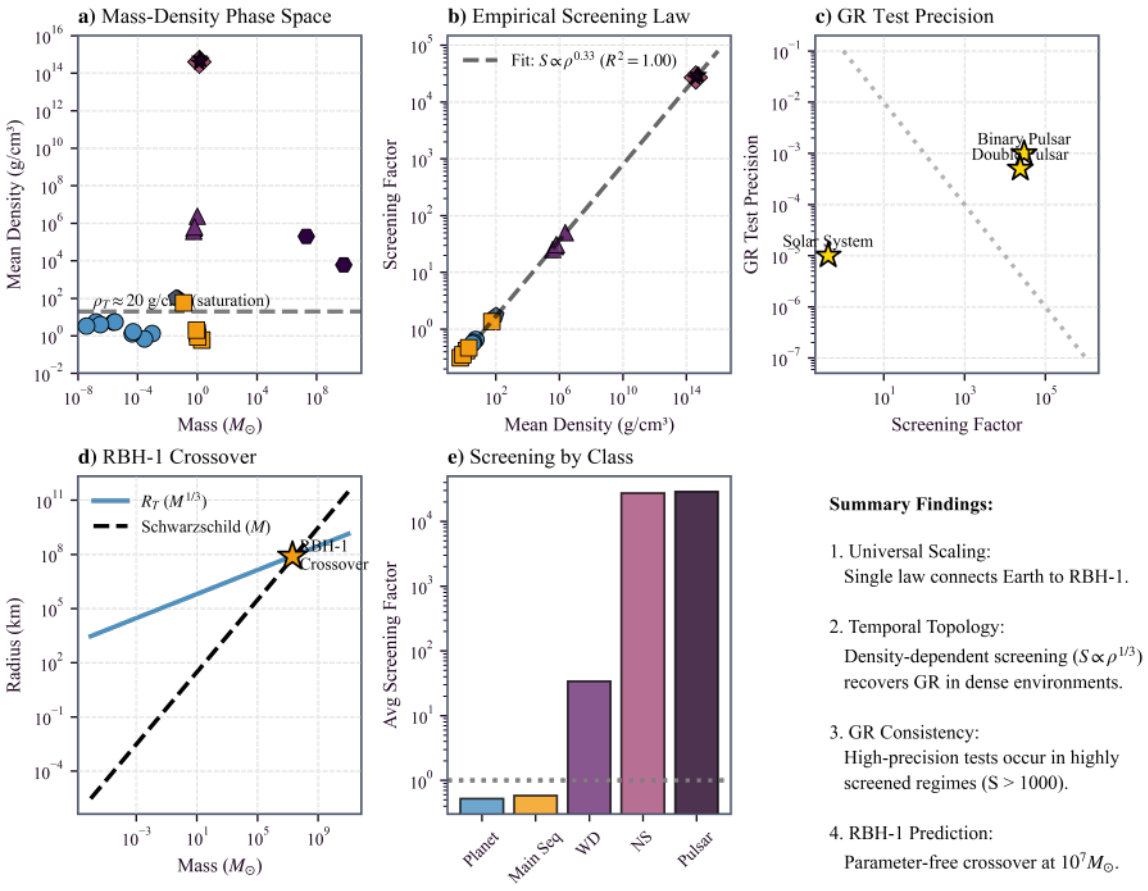

Figure C.3: Comprehensive Screening Analysis. (A) Mass-density phase space spanning 60 orders of magnitude. (B) Empirical screening law: $S \propto \rho^{0.334}$. (C) Screening hierarchy and regime separation across densities. (D) Cross-regime consistency with the universal density $\rho_T \approx 20$ g/cm³.

Appendix D: EHT Soliton Detection — Sensitivity and Feasibility

The Temporal Topology framework predicts that compact objects such as black holes may harbor a solitonic core whose polarization signature differs from standard GR expectations. Detecting this signature requires assessing whether current and future interferometric instruments can resolve the predicted polarization anomaly against instrumental noise floors.

ρ_T Constraint on the Soliton Core Size

The central constant of this paper, $\rho_T \approx 20$ g/cm³, sets the physical scale of the soliton core directly via the saturation radius:

$$R_T = \left(\frac{3M}{4\pi\rho_T} \right)^{1/3}. \tag{34}$$

For the two primary EHT targets, this yields:

Target	Mass	Predicted R_T	Physical Size (R_{phys})	Screening $S = R_T/R_{\text{phys}}$
M87*	$\sim 6.5 \times 10^9\, M_\odot$	≈ 3.6 AU (5.4×10^8 km)	$\approx 1.9 \times 10^{10}$ km	~ 0.03 (unscreened)
Sgr A*	$\sim 4.3 \times 10^6\, M_\odot$	≈ 0.3 AU (4.7×10^7 km)	$\sim 10^7$ km	~ 4.7 (screened)

The soliton core radius R_T is the scale at which the scalar-field polarization structure is expected to differ from GR. For **M87***, the predicted $R_T \approx 3.6$ AU corresponds to an angular scale of $\sim 4\,\mu$as at 16 Mpc — well below the EHT's $\sim$20 μas spatial resolution at 230 GHz, but potentially accessible through the polarization signal described below. The small screening factor ($S \sim 0.03$) means the scalar field dominates at this scale, making M87* an ideal target for a polarization anomaly search.

For **Sgr A***, the predicted $R_T \approx 0.3$ AU corresponds to $\sim 4\,\mu$as at 8 kpc, also below the EHT beam. However, the screening factor is substantially larger ($S \sim 4.7$), meaning the scalar contribution is partially suppressed. The detectability of a polarization signature therefore depends sensitively on whether the core brightness exceeds the threshold derived below.

Polarization Signature Model

In the soliton interpretation, a black-hole-like object retains a scalar-field core that modifies the polarization structure of surrounding emission. The observable is the fractional polarization $m_{\rm obs}$ of core emission, which depends on two parameters:

- **Core relative brightness** $b_{\rm rel}$: the ratio of core to ring peak intensity.
- **Intrinsic core polarization** $p_{\rm int}$: the fraction of core flux that is polarized.

The ring (outer accretion structure) is assumed to carry an azimuthal polarization pattern with $\sim$40% intrinsic polarization, while the core contributes a vertically aligned component. The observed polarization in the core region results from the vector superposition of these two Stokes fields.

Feasibility Analysis

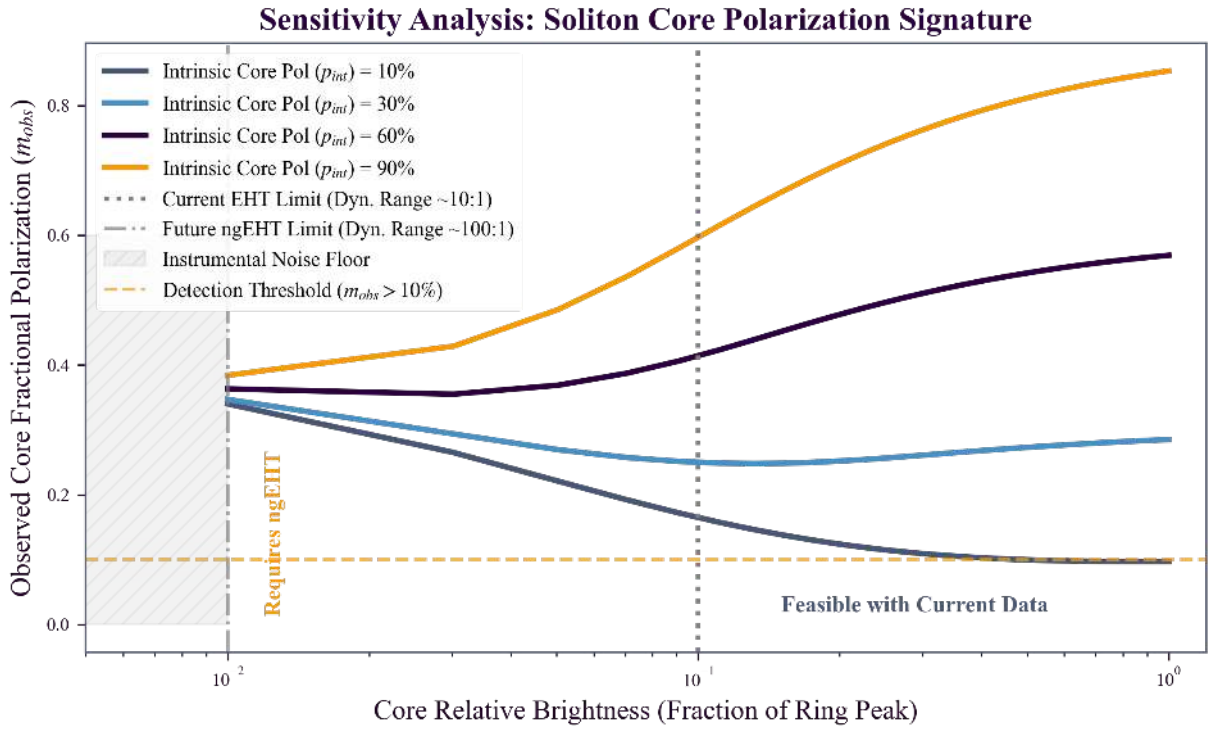

Figure 8. *Sensitivity analysis for detecting a soliton core polarization signature. Curves show the observed fractional polarization $m_{\rm obs}$ in the core region as a function of core relative brightness, for four intrinsic polarization levels (10%, 30%, 60%, 90%). The horizontal dashed line marks a 10% detection threshold. Vertical lines indicate current EHT dynamic-range limits (∼10:1) and projected ngEHT limits (∼100:1). Regions left of the current limit require future instrumentation.*

The analysis shows that for cores with $p_{\rm int} \gtrsim 30\%$ and relative brightness $b_{\rm rel} \gtrsim 0.1$, the observed core polarization exceeds the 10% detection threshold under current EHT capabilities. For fainter cores ($b_{\rm rel} \lesssim 0.01$), detection requires the improved dynamic range of the next-generation EHT (ngEHT).

Key Results

Current EHT Feasibility

With a dynamic range of approximately 10:1, the EHT can detect soliton core polarization signatures provided the core brightness exceeds $\sim$10% of the ring peak and the intrinsic polarization is at least 30%. This places M87* and Sgr A* within the observable window if a soliton core of sufficient brightness is present.

Future ngEHT Reach

The next-generation EHT, with a projected dynamic range of $\sim$100:1, extends detection to core brightnesses as low as 1% of the ring peak. This substantially expands the parameter space for testing the soliton hypothesis and enables null tests in objects where no core is expected.

Testable Predictions

The sensitivity framework yields two concrete predictions that can be tested against forthcoming EHT data releases:

1. **Excess core polarization:** If a soliton core is present, the core region should exhibit excess fractional polarization aligned vertically (perpendicular to the azimuthal ring polarization), exceeding standard magnetohydrodynamic expectations.
2. **Null tests in confirmed GR objects:** For black holes where GR is known to hold to high precision (e.g., through binary pulsar tests), the absence of a core polarization anomaly constrains the scalar-field coupling strength.

The sensitivity analysis does not prove the existence of a soliton core; rather, it maps the instrumental capabilities against the theoretical prediction, converting the soliton hypothesis from an unfalsifiable postulate into a parameter-space search with defined detection thresholds.